Chapter 5

The Effects of Ballistic Accretion on a Protobinary System

In Chapter 4, a method for following the accretion of gas on to a protostellar system using SPH was presented. This technique is used in the remainder of this thesis to study the effects of accretion during the formation of a binary system. As discussed in Sections 1.4 and 4.1, the 'seed' binaries formed in fragmentation calculations initially only contain a fraction of the original cloud's mass. The accretion of the rest of the cloud on to this protobinary thus determines the final state of the system.

In this chapter, the effects of accretion on the parameters of a protobinary system are studied by considering simple ballistic accretion of particles. A 'seed' binary is placed at the centre of a cloud of 'gas'. The 'gas' is modelled by particles which fall on to the protostars and are accreted. The masses of the protostars are M_1 and M_2 for the primary and secondary respectively, and the system has separation a, and eccentricity e. Initially, the binary separation is $a = D$ and the binaries are circular ($e = 0$). The 'gas' particles are non-self-gravitating, with a mass very much less than that of the binary, and all pressure and viscous forces between particles that would be present in a full SPH simulation are neglected. The effects of this accretion on the mass ratio and separation of the binary are studied. This method was used by Artymowicz (1983) and a summary of his conclusions are given in Section 1.4.2. He found the results depended primarily on the initial mass ratio of the binary and the specific angular momentum of the cloud material. The results were not found to depend significantly on the radial-infall velocity of the particles at the outer boundary of the calculation, or upon the relative sizes of the protostars.

In this chapter, ballistic accretion calculations are performed to cover a much larger parameter space of binary mass ratios (from $q = M_2/M_1 = 0.1 - 1.0$) than Artymowicz studied. The dependence of the results on the sizes of the protostars relative to their separation is also investigated in more detail. Finally, the spin angular momentum accreted by the protostars is also considered. In gaseous accretion calculations this is important for circumstellar disc formation.

Following this ballistic study, in Chapter 6, gaseous accretion is considered, with pressure and viscous forces between particles included. The results from ballistic accretion and gaseous accretion are then compared and contrasted.

5.1 Method

For the study of ballistic accretion, a cut-down version of the full SPH code is used. Much of the SPH code can be removed, saving both time and memory. In particular, no inter-particle forces are required, eliminating the need to build a tree. The particles are acted upon by gravitational forces from the binary only. The time step for the integration of their orbits is controlled only by the Runge-Kutta-Fehlberg integrator tolerance (Equation 2.48).

The protostars are modelled by sink particles as described in Chapter 4. As there are no pressure or viscous forces, the boundary conditions described in Section 4.2.3 are not required. Also, as there is no dissipation of the energy of infalling particles via viscosity, the requirements for a particle to be accreted by a sink particle (Section 4.2.1) are ignored. Instead, a sink particle accretes any particle that enters its accretion radius. The results are, therefore, expected to depend on the accretion radii of the sink particles. This dependence is investigated.

Each calculation is begins with 5000 'gas' particles of equal mass modelling the cloud. When a particle is accreted by one of the protostars, it is randomly assigned a new position at the outer boundary of the calculation region and given a new velocity. As accretion of ballistic particles is being considered, it is also possible for particles to be expelled via a three-body interaction with the binary. To maintain a cloud of 5000 particles, any particle that leaves the simulation region is removed and its position and velocity are reassigned as for an accreted particle. The calculations are evolved until all memory of the initial conditions is lost, and steady-state accretion on to both protostars is established. At this point, the accretion rates and effects on the binary's orbital parameters are calculated.

5.1.1 Initial Conditions and Particle Reassignment

The initial distribution of the cloud and the method for reassigning a particle's position and velocity once it is accreted or removed must now be specified. Only accretion from a cloud with the same axis of rotation as that of the binary is considered. The cloud is either stationary, or is rotating in the same sense as the binary. Accretion from retrograde clouds is not studied. These assumptions are justified as it is envisaged that the infalling gas is from the cloud that the protobinary formed out of.

Artymowicz (1983) found the effects of accretion vary mainly with the specific angular momentum of the cloud material. Because of this, we specify that a given simulation has each particle injected with the same specific angular momentum j. Thus, a particle's initial tangential velocity around the centre of mass is $v_{\rm t} = j/r_{\rm xy}$, where $r_{\rm xy}$ is the cylindrical radius from the axis of rotation of the binary. Due to the rotation of the

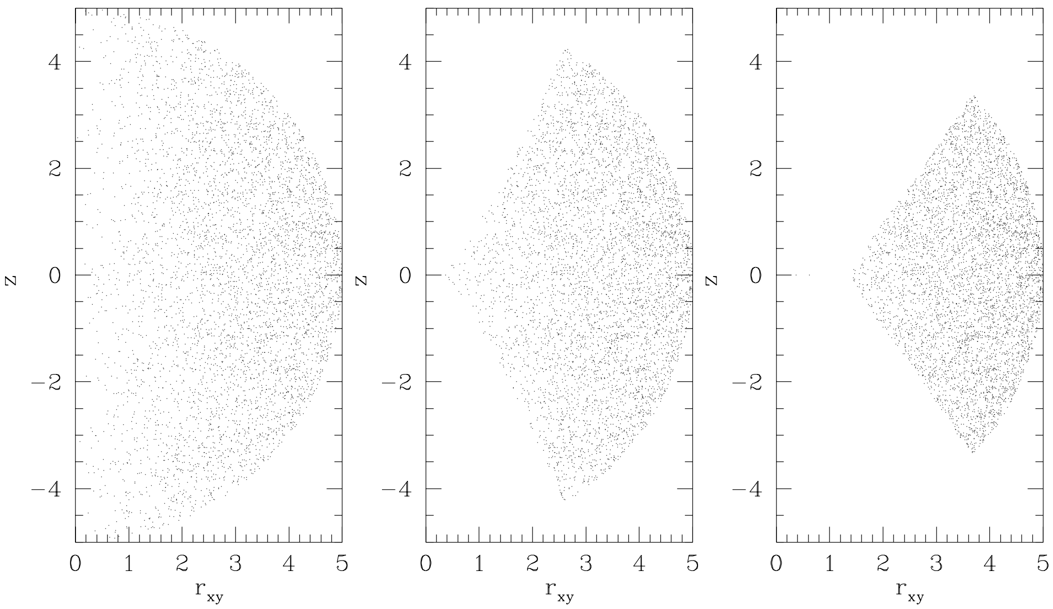

Figure 5.1: The initial particle distributions for calculations of ballistic accretion from envelopes with specific angular momenta of $j = 0$ (left), $j = 0.6$ (centre), and $j = 1.2$ (right) surrounding a protobinary. For a stationary cloud the distribution is spherical. As the specific angular momentum is increased, particles are absent near the poles as the gravitational forces on them would be exceeded by centrifugal forces. Distance is expressed in units of the initial binary separation D.

cloud, each particle has a centrifugal acceleration acting upon it. Clearly, any position in the cloud for which the centrifugal acceleration is not balanced or exceeded by the acceleration due to gravity of the binary should not initially be occupied by gas as it would not have been able to fall into this region from farther out in the cloud. Thus, we set the initial 'gas' particle positions to be randomly distributed within a sphere of radius R, such that

$$\frac{v_{\rm t}^2}{r_{\rm xy}} \leq \frac{GM_{\rm b}}{r^2}\frac{r_{\rm xy}}{r} \tag{5.1}$$

where the mass of the binary $M_{\rm b} = M_1 + M_2$, and r is the radius of a particle from the centre of mass of the binary. In the case of a stationary cloud, the whole sphere is filled. As the angular momentum of the cloud is increased, a cone-shaped hole in the particle distribution appears above and below the orbital plane of the binary. Several different particle distributions are shown in Figure 5.1.

As particles are accreted by the binary, or expelled out to a radius greater than the outer boundary of the calculation R, they are assigned new positions and velocities to maintain the cloud of infalling particles. We assign them new positions over the surface of the sphere of radius R, such that they have a uniform-density distribution modified by Equation 5.1. Thus, for $j > 0$, the poles of the sphere receive no particles. Most calculations have the outer boundary of the calculation equal to five times the initial binary separation $R = 5D$.

In addition to the tangential velocity, the radial-infall velocity of reassigned particles can be varied. This is set as some fraction $v_{\rm rad}$, of the radial velocity a particle would have after a free-fall from infinity

$$v_{\rm r} = v_{\rm rad}\sqrt{\frac{2GM_{\rm b}}{r} - \frac{j^2}{r_{\rm xy}^2}} \tag{5.2}$$

where it is assumed for $v_{\rm rad} = 1$ that the kinetic energy of the particle is equal to the gravitational energy liberated during its fall. The effect of varying $v_{\rm rad}$ is studied by running many simulations with both $v_{\rm rad} = 0$ and $v_{\rm rad} = 1$. Note that increasing the cloud radius, while keeping $v_{\rm rad} = 0$, has the same effect as maintaining the same cloud radius and increasing $v_{\rm rad}$.

A total of 276 calculations were performed, varying the initial mass ratio of the binary, the cloud's angular momentum, the accretion radii of the sink particles (protostars), and the radial-infall velocity at the outside of the cloud. A few simulations were also performed to confirm that the results are scale-free under increase of the binary separation, increase of the total mass of the binary, and increase of the mass of the 'gas' particles. The accretion rates increase linearly with the total mass of the binary, and with the mass of the 'gas' particles, as expected. Also, the results for the relative accretion rate on to the binary components are the same, within statistical errors, for simulations where the separation of the binary is increased by a factor f, and the angular momentum of the cloud is increased in proportion to $\sqrt{f}$. In these cases, the accretion radii of the sink particles is also increased by f.

5.1.2 Example Simulations

For the remainder of this chapter, all the times are given in units of

$$t = \sqrt{\frac{D^3}{GM_{\rm b}}}, \tag{5.3}$$

and we set $G = 1$, and initially $M_{\rm b} = 1$ and $D = 1$. For this choice of units, a specific angular momentum of unity corresponds to the specific angular momentum j that a 'gas' particle requires to form a circular orbit (in the absence of gravitational torques from the binary) about the centre of mass of the binary at a radius equal to the separation (i.e. $j_{\rm circ} = \sqrt{GM_{\rm b}D} = 1$). For all simulations, each of the 5000 'gas' particles has a mass of $m = 10^{-6}M_{\rm b}$.

The results from two simulations are presented as examples of how the simulations are analysed. The first is the ballistic accretion of a stationary cloud ($j = 0$) on to a $q = 0.6$ protobinary. In the second simulation, high-angular-momentum material ($j = 1.2$) is accreted on to a $q = 0.6$ protobinary. In both simulations, $v_{\rm rad} = 0$ and the accretion radius of each protostar is $r_{\rm acc} = 0.05D$.

Figure 5.2 gives the results for the stationary case. The masses of the primary and secondary as a function of time are given in Figures 5.2a and 5.2b respectively. Except

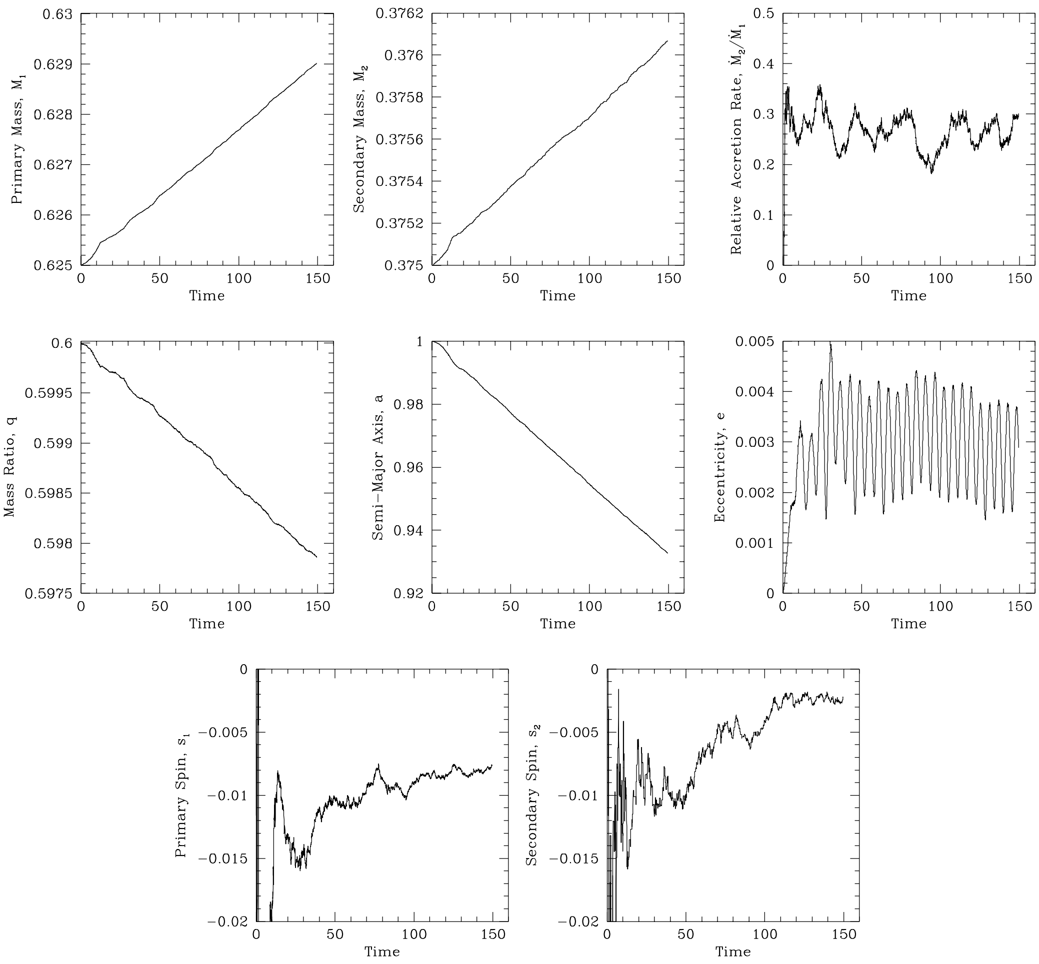

Figure 5.2: The effects of zero-angular-momentum, ballistic accretion on an embedded $q = 0.6$ 'seed' binary. Plotted, as a function of time, are a) the mass of the primary M_1 (top, left); b) the mass of the secondary M_2 (top, centre); c) the relative accretion rate $\dot{M}_2/\dot{M}_1$ (top, right); d) the mass ratio q (centre, left); e) the separation a (centre); f) the eccentricity e (centre, right); g) the specific spin angular momentum of the primary s_1 (bottom, left); h) the specific spin angular momentum of the secondary s_2 (bottom, right). The calculation has $v_{\rm rad} = 0$.

for a short time at the beginning of the simulation, the accretion rates are steady, with all memory of the initial conditions being lost. The mass ratio (Figure 5.2d) is decreasing with time, and again demonstrates the accretion flow reaches steady-state soon after the beginning of the simulation. Figure 5.2e gives the semi-major axis separation of the binary which is also decreasing. Despite the fact that the separation decreases by 7% over the entire simulation, the accretion rates are constant. This is to be expected for zero-angular-momentum infall, assuming the effect of a finite accretion radius for the protostars is small. The eccentricity of the system is given in Figure 5.2f. A small eccentricity grows at the beginning of the simulation. For all simulations, however, the eccentricity remains less than $e = 0.006$ throughout. As eccentricity is always positive, any force on the binary produces a non-zero eccentricity. Thus, as soon as a particle is

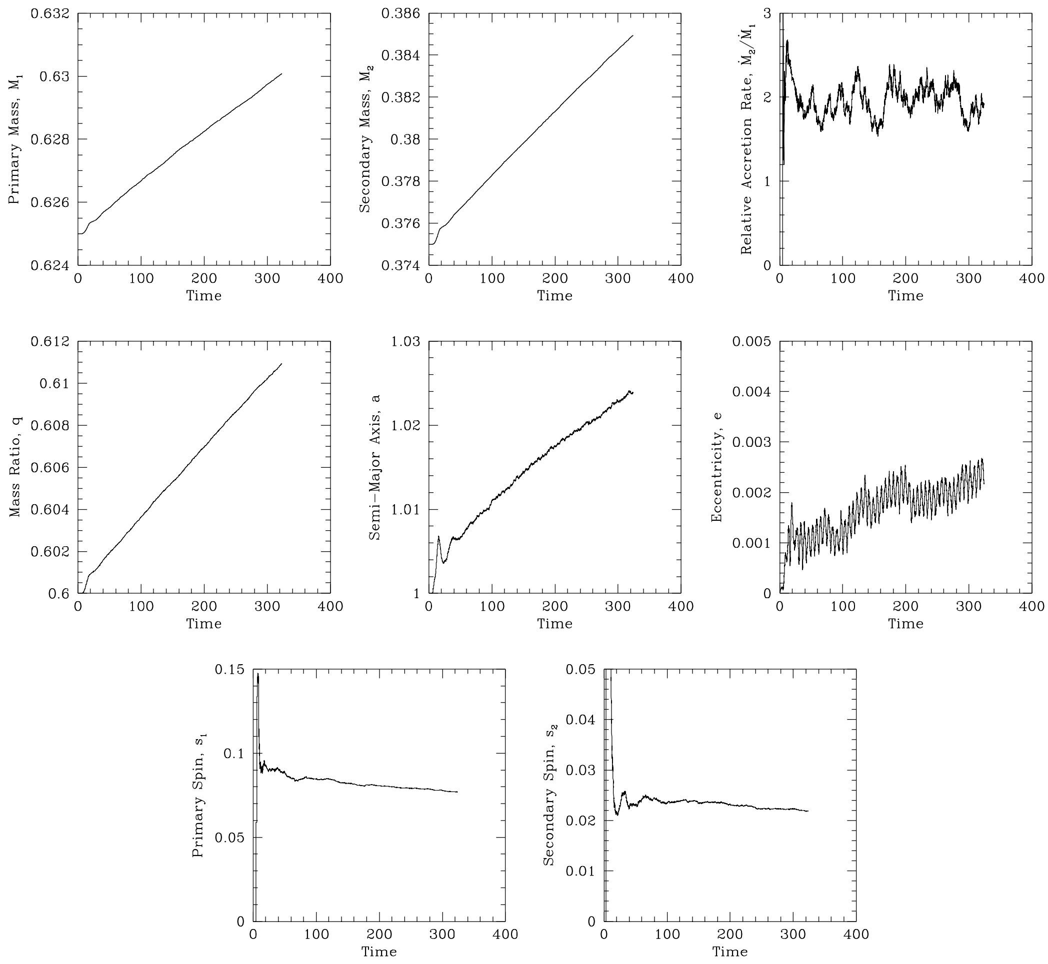

Figure 5.3: The effects of high-angular-momentum, ballistic accretion ($j = 1.2$) on an embedded $q = 0.6$ 'seed' binary. See Figure 5.2 for details.

accreted, giving mass and momentum to the protostar, the eccentricity is non-zero. The sine-shaped oscillation of the eccentricity was noted by Artymowicz (1983). The period of the oscillation is equal to the orbital period of the binary. Such periodic changes of orbital elements are known from analytic solutions of binary motion under a perturbing force (Kopal 1959). Finally, the specific spin angular momenta accreted by the primary s_1 and secondary s_2 are given in Figures 5.2g and 5.2h, respectively. Very little spin angular momentum is accreted by either component, though more is accreted by the primary. The spin is also in the opposite sense to that of the binary.

With accretion from a cloud with high angular momentum, as in Figure 5.3, the initial conditions affect the results for longer before all memory of them is lost. Three-body encounters with the binary and accretion of particles take longer to erase memory of the initial conditions for two reasons. First, the particles take longer to fall in due to centrifugal forces. Second, the particles have high angular momentum and thus many do not fall in far enough to undergo a strong interaction with the binary and are expelled out to the boundary and reassigned. With zero-angular-momentum infall, the particles quickly fall into the centre and encounter the binary. This interaction erases the memory of the initial conditions rapidly. A steady-state is for the high-angular-momentum infall is eventually reached, however. In this case, the secondary accretes material faster than the primary, and the mass ratio increases with time (Figure 5.3d). The binary also gains specific orbital angular momentum from the cloud, and thus its separation increases (Figure 5.3e). The eccentricity shows the same general behaviour as in the zero-angular-momentum case, although the amplitude of the oscillations is reduced. This occurs in general - the oscillations of eccentricity display no noticeable dependence on the mass ratio of the binary, or the accretion radii of the components, but the amplitude decreases with increasing angular momentum of the cloud. The spin accreted by the protostars is still greater for the primary than for the secondary, but this time the spins are large and in the same sense as the binary's and cloud's rotation.

For each simulation, the effects of accretion on the masses and orbit of the protostars are determined by linear regressions of the accretion rates, mass ratio, and separation as functions of time. The linear regressions are done over the period of steady-state accretion only. This provides the accretion rates $\dot{M}_1$, and $\dot{M}_2$, and the rates of change of the mass ratio $\dot{q}$ and the semi-major axis $\dot{a}$. Error estimates for each of these are obtained from the linear regression. For the accretion rates, the linear regression errors are combined with $\sqrt{N}/N$ statistical errors, where N is the number of particles accreted over the time period. These errors provide a good estimate of the true errors in the quantities. A second calculation of the rate of change of the mass ratio can be found, with a better estimate of errors, from

$$\dot{q} = (\dot{M}_2 - q\, \dot{M}_1)\frac{(1+q)}{M_{\rm b}}. \tag{5.4}$$

Note that this means the mass ratio increases if

$$\frac{\dot{M}_2}{\dot{M}_1} > q, \tag{5.5}$$

and not simply when $\dot{M}_2 > \dot{M}_1$. The values of the specific spin angular momentum of the primary and secondary are taken at the end of the simulations when they attain constant values, again with statistical errors.

With ballistic accretion, many particles are ejected from the cloud due to three-body encounters. Thus, the total accretion rate on to the binary varies between each simulation, as the number of particles lost compared to those accreted varies. Also, with the variation of the angular momentum of the particles, the infall rate on to the system also varies. A less confusing representation of the effects of accretion is obtained if the above quantities are normalised by the total accretion rate on to the binary $\dot{M}_{\rm b} = \dot{M}_1 + \dot{M}_2$. Hence, the quantities $\dot{q}/\dot{M}_{\rm b}$, $\dot{a}/\dot{M}_{\rm b}$ are used during much of the following analysis. Since initially $a = 1$ and $M_{\rm b} = 1$, then $\dot{M}_{\rm b}$ and $\dot{a}$ are also the fractional changes in $M_{\rm b}$ and a with time. Thus, $\dot{q}/\dot{M}_{\rm b} = \dot{q}/(\dot{M}_{\rm b}/M_{\rm b})$ and $\dot{a}/\dot{M}_{\rm b} = (\dot{a}/a)/(\dot{M}_{\rm b}/M_{\rm b})$.

5.2 Effects of Ballistic Accretion on Binary Masses

We now consider the effects of accretion on the masses of the binary's components. First, the mass accreted by each component is considered separately. Second, the relative accretion rate and its effect on the mass ratio are considered.

The results cover mass ratios from $q = 0.1 - 1.0$ in intervals of 0.1, with the angular momentum of the cloud varying from $j = 0.0 - 1.4$ in each case. The dependence of the results on the sizes of the protostars is investigated by performing calculations with $r_{\rm acc} = 0.05D$ and with $r_{\rm acc}$ equal to the mean-Roche-lobe sizes of the protostars. The mean-Roche-lobe sizes of the protostars are taken to be (Frank, King & Raine 1985)

$$R_1/a = 0.38 - 0.20 \log q, \qquad 0.05 < q < 2.0, \tag{5.6}$$

for the primary and

$$\begin{aligned} R_2/a &= 0.38 + 0.20 \log q, \qquad 0.5 \leq q < 20, \\ R_2/a &= 0.462\ (q/(1+q))^{1/3}, \quad 0 < q < 0.5, \end{aligned} \tag{5.7}$$

for the secondary. These two cases are extremes that the true protostellar sizes should lie between. For example, although for a binary with an intermediate or wide separation the physical sizes of the protostars may be very much less than the separation, the formation of circumstellar discs around the two components may increase their effective sizes to be similar to the Roche-lobe size. Finally, for each case with $r_{\rm acc} = 0.05D$, the calculations are performed with both $v_{\rm rad} = 0$ and $v_{\rm rad} = 1$ to investigate the sensitivity of the results to the radial-infall velocity of the cloud material at the outer boundary of the calculations. With the mean-Roche-lobe-sized protostars, the calculations have $v_{\rm rad} = 1$.

5.2.1 Accretion Rates

The accretion rates on to each of the protostars are given in Figures 5.4 to 5.13. The results are displayed for each mass ratio q separately, as a function of the cloud's specific angular momentum j. The accretion rate on to each component $\dot{M}_1$, $\dot{M}_2$ and the total accretion rate on to the binary $\dot{M}_{\rm b}$ are given.

Considering low-mass-ratio binaries, it is found that the primary and secondary's accretion rates reach maximums at different values of the specific angular momentum of the infalling cloud. This can be understood if the orbits of the infalling particles are considered. Since the particles fall from a radius R then, taking the simplification of replacing the binary by a single point mass, their orbits take them back out to that radius again. If $v_{\rm rad} > 0$, or if the particles gain some energy from the encounter with the binary, their apastron distance will be greater than the cloud radius R and the particles are removed. Thus, most particles have only one pass of the binary in which to be accreted.

Keeping this in mind, for low-angular-momentum infall, most particles fall approximately radially toward the centre of mass of the binary. With a low-mass-ratio binary,

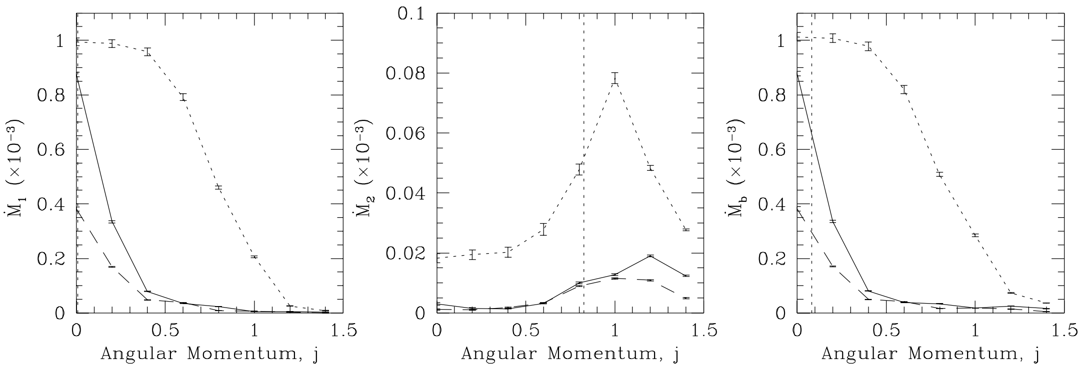

Figure 5.4: Effect of accretion on binary masses for a $q = 0.1$ binary. Graph a) gives the primary's accretion rate $\dot{M}_1$; graph b) gives the secondary's accretion rate $\dot{M}_2$; and graph c) gives the accretion rate of the binary $\dot{M}_{\rm b}$. The different curves are for: $r_{\rm acc} = 0.05D$ and $v_{\rm rad} = 1$ (solid); $r_{\rm acc} = 0.05D$ and $v_{\rm rad} = 0$ (dashed); $r_{\rm acc}$ equal to the mean-Roche-lobe radii and $v_{\rm rad} = 1$ (dotted). Estimated error bars are given. The vertical lines give the specific orbital angular momentum of the primary (graph a), or the secondary (graph b) (dotted). In graph c) the vertical line gives the specific angular momentum of the binary system (dotted).

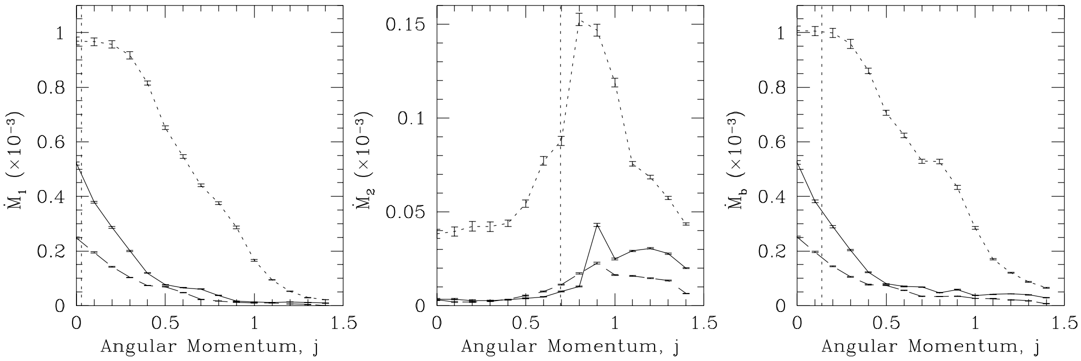

Figure 5.5: Effect of accretion on binary masses for a $q = 0.2$ binary. See Figure 5.4 for details.

these particles are mainly accreted by the primary, which is close to the centre of mass of the system (e.g. Figure 5.4a). This is especially true for the mean-Roche-lobe-accretion-radius calculations. For the small-accretion-radius calculations, many also gain energy in the encounter with the primary, avoid accretion, and escape from the system. Very few particles pass close to the secondary and are accreted by it (e.g. Figure 5.4b), especially for small-accretion-radius calculations.

With higher-angular-momentum infall, however, the particles fall on elliptical orbits with their periastron dependent on their initial angular momentum and energy. They no longer fall into the centre of mass of the binary, occupied by the primary, but instead to some larger radius. The primary can only accrete material that loses angular momentum and energy allowing it to fall in to a smaller radius. This only happens to

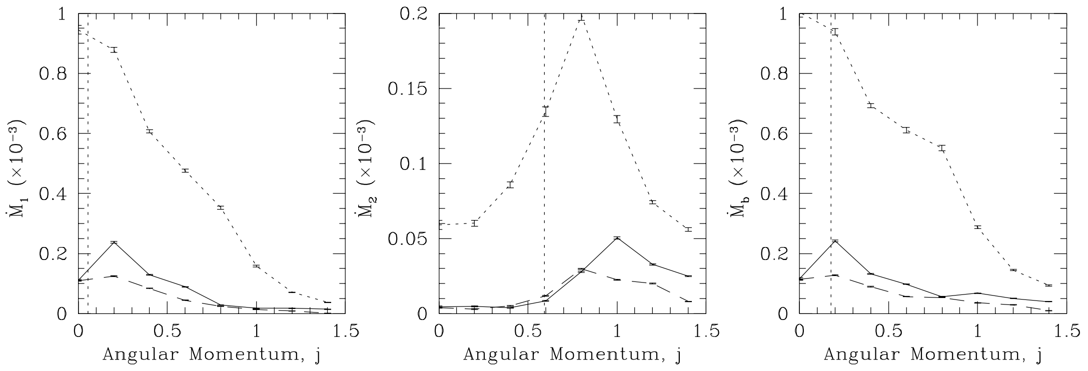

Figure 5.6: Effect of accretion on binary masses for a $q = 0.3$ binary. See Figure 5.4 for details.

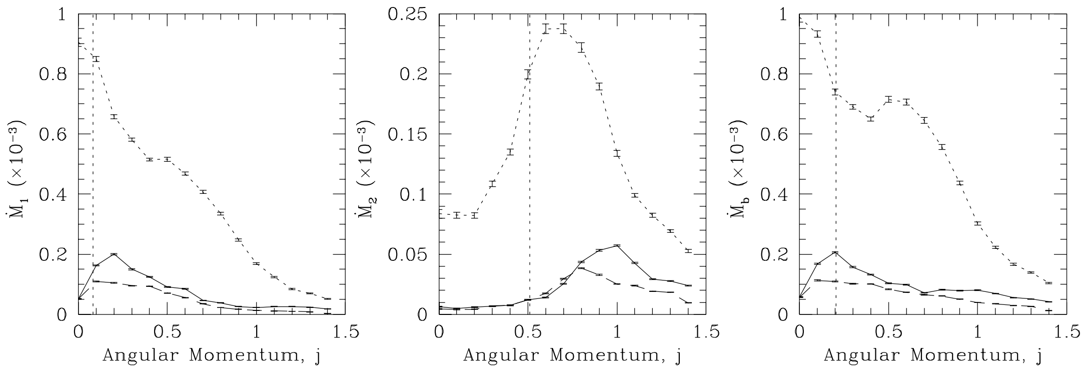

Figure 5.7: Effect of accretion on binary masses for a $q = 0.4$ binary. See Figure 5.4 for details.

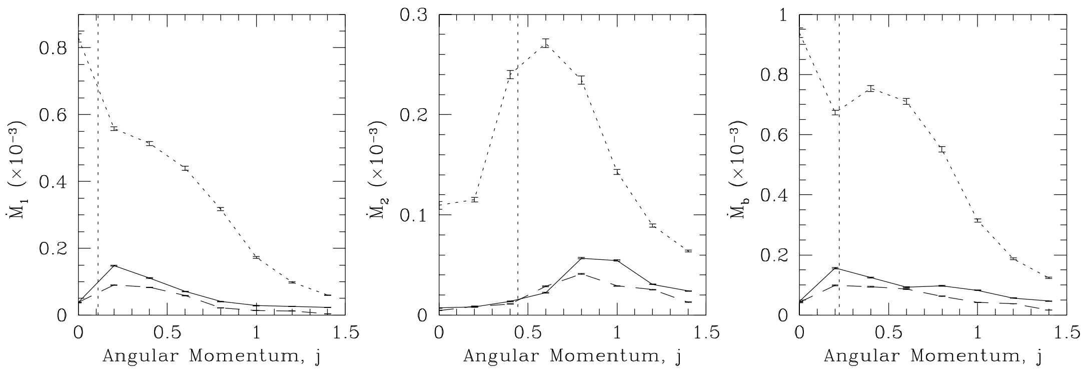

Figure 5.8: Effect of accretion on binary masses for a $q = 0.5$ binary. See Figure 5.4 for details.

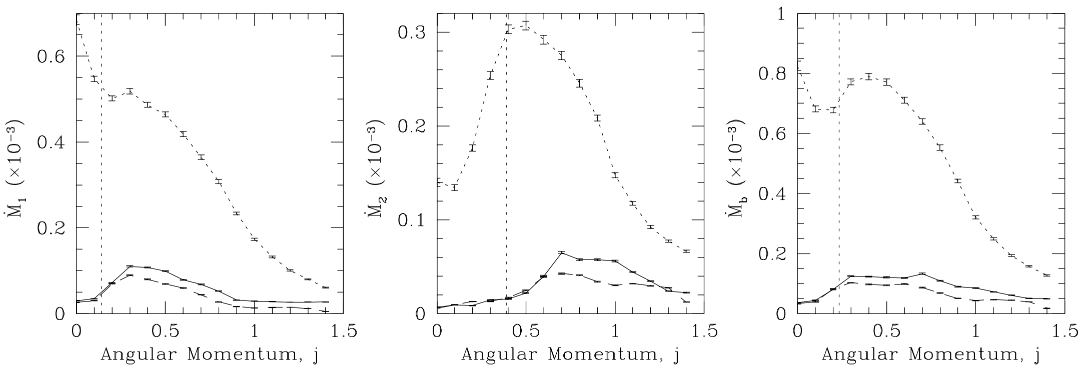

Figure 5.9: Effect of accretion on binary masses for a $q = 0.6$ binary. See Figure 5.4 for details.

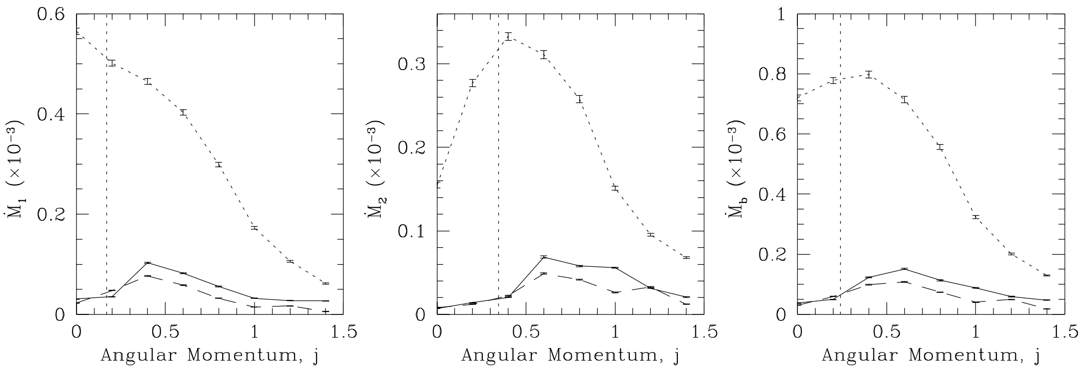

Figure 5.10: Effect of accretion on binary masses for a $q = 0.7$ binary. See Figure 5.4 for details.

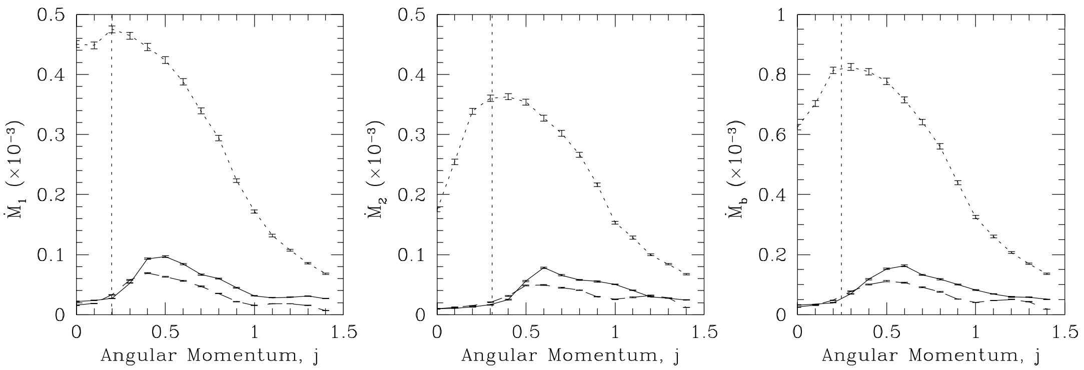

Figure 5.11: Effect of accretion on binary masses for a $q = 0.8$ binary. See Figure 5.4 for details.

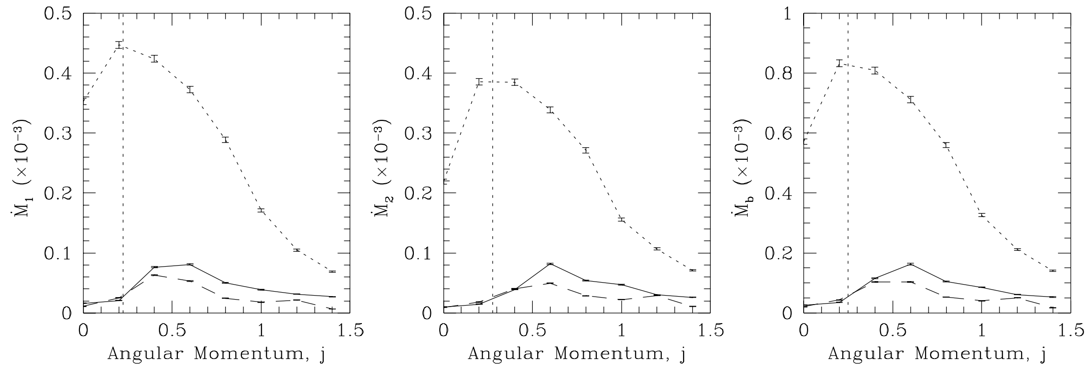

Figure 5.12: Effect of accretion on binary masses for a $q = 0.9$ binary. See Figure 5.4 for details.

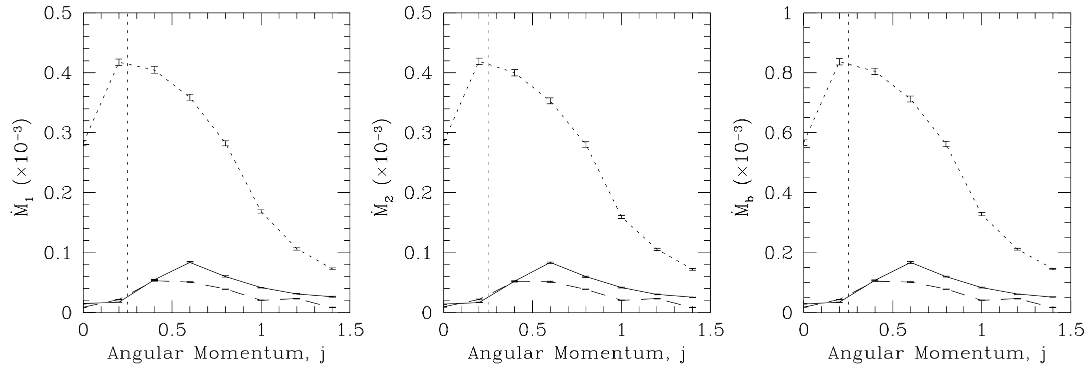

Figure 5.13: Effect of accretion on binary masses for a $q = 1.0$ binary. See Figure 5.4 for details.

a fraction of the infalling material as the torques exerted by the low-mass secondary are small. Also, as j increases, the amount of material that is perturbed to fall near the primary decreases. Most of the material falls in, passes periastron, and travels out to be removed at the outer boundary. The secondary can accrete more high-angular-momentum material than low-angular-momentum material (Figure 5.4b), as it has a specific orbital angular momentum j_2 closer to the specific angular momentum of the infalling material (and hence similar orbital velocity) and this makes capture easier. The specific orbital angular momentum of the primary and secondary are given by

$$j_1 = \sqrt{GM_{\rm b}a}\frac{q^2}{(1+q)^2}, \tag{5.8}$$

and

$$j_2 = \sqrt{GM_{\rm b}a}\frac{1}{(1+q)^2}, \tag{5.9}$$

respectively. In addition, for higher-angular-momentum infall, the material is confined to be closer to the orbital plane of the binary (Section 5.1.1 and Figure 5.1). Thus, more of the cross-section of the infall is covered by the secondary than with lower j infall. This also explains why the peak in both the primary's and secondary's accretion rates tend to occur at higher j for the small-accretion-radii calculations.

This increased accretion by the secondary does not balance the loss in accretion by the primary (Figure 5.4c), however, since the gravity of the secondary is less than that of the primary, and its orbit is much larger than the primary's, so much of the material falling into its radius from the centre of mass is relatively unaffected and is allowed to escape. These affects result in a decrease in the total accretion rate $\dot{M}_{\mathrm{b}}$ on to the system with increasing angular momentum.

As the mass ratio of the binary is increased, a peak in the graph of $\dot{M}_{\mathrm{b}}$ versus angular momentum appears (e.g. Figure 5.11c), especially for the small-accretion-radius cases. This is because accretion on to both the primary and the secondary components is at a maximum when $j > 0$ as the primary also moves away from the centre of mass of the system.

The combinations of accretion on to the primary and secondary give a single peaked $\dot{M}_{\mathrm{b}}$ versus j distribution for all mass ratios, except those with $q \approx 0.5$ (see Figure 5.8c). For small mass ratios, the accretion on to the primary dwarfs the secondary's accretion rate. For large mass ratios, the values of the angular momentum which give peak accretion rates for each of the components become equal as their distances from the centre of mass of the system become equal, giving a single peak in $\dot{M}_{\mathrm{b}}$. The effect of a higher initial radial-infall velocity is typically to increase the accretion rate on to the system, since the particles travel in quicker.

Finally, the effect of increasing the accretion radii of the protostars acts to increase the accretion rates on to both the components as more particles intersect the accretion radii. It also broadens the accretion rate peaks for the primary and secondary, as particles do not have to match the protostars' angular momenta as closely to be accreted. The effect of varying the accretion radius is studied in more detail in Section 5.2.3.

In Chapter 6, when pressure and viscous forces are added to simulate gaseous accretion, these differences in the total accretion rate on to the system are eliminated because particles are no longer expelled. Instead, they lose energy by viscous interactions with other streams. The binary accretion rate does vary due to circumbinary disc formation for high j, but all the infalling material remains bound to the system.

5.2.2 Relative Accretion Rate and Rate of Change of Mass Ratio

In all cases then, the maximum accretion on to each component of the system occurs at a value of j that increases with the distance of the component from the centre of mass of the binary. The result of this is that the maximum and minimum relative accretion rates are most extreme for low-mass-ratio binaries (Figures 5.14a to 5.23a). This is accentuated by the relative gravitational fields. For low-angular-momentum infall, the primary has the largest gravitational field and will attract more material regardless of its position. For high-angular-momentum infall, the secondary's lower gravity is less likely to remove angular momentum from particles to allow them to fall in and be accreted by the primary, and they are expelled instead. For accretion on to a low-mass-ratio binary, the relative accretion rate can vary between ≈ 0.003 and ≈ 10 depending on the

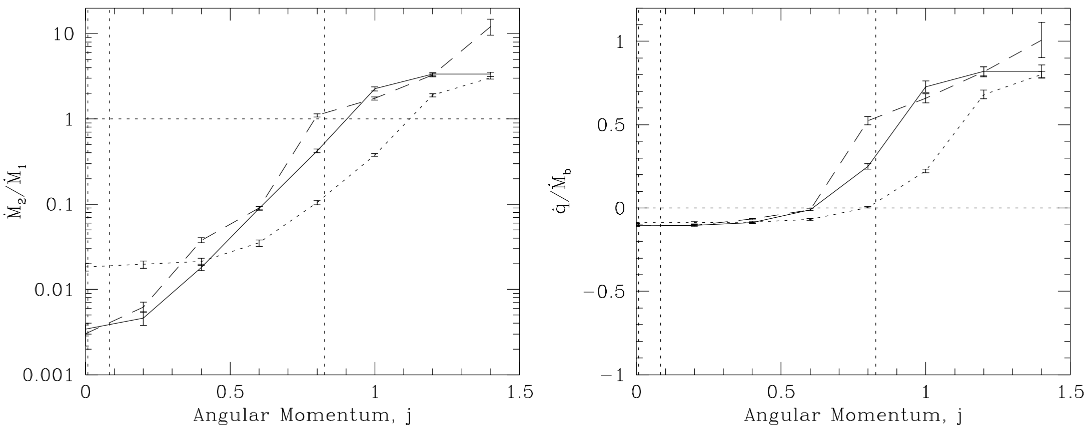

Figure 5.14: Effect of accretion on binary masses for a $q = 0.1$ binary. Graph a) gives the relative accretion rate $\dot{M}_2/\dot{M}_1$ (left), and graph b) gives the rate of change of mass ratio per fractional mass accreted by the system $\dot{q}/\dot{M}_{\rm b}$ (right). The different curves are for: $r_{\rm acc} = 0.05D$ and $v_{\rm rad} = 1$ (solid); $r_{\rm acc} = 0.05D$ and $v_{\rm rad} = 0$ (dashed); $r_{\rm acc}$ equal to the mean-Roche-lobe radii and $v_{\rm rad} = 1$ (dotted). Estimated error bars are given. The vertical lines give the specific orbital angular momentum of the primary (left), the binary (middle), and the secondary (right).

angular momentum of the infalling material and the sizes of the protostars! As already observed, for low-angular-momentum infall the primary accretes most of the material, while for high-angular-momentum material the secondary accretes most. As the mass ratio is increased, the relative accretion rates become less extreme and converge to unity for $q = 1$. Note that for the small-accretion-radii calculations, the value of the cloud's angular momentum for which the relative accretion rate is unity is almost **independent** of the mass ratio. The relative accretion rate is unity when $j \approx 0.7 - 0.8$. This is not the case for the mean-Roche-lobe-sized calculations. Further discussion of this observation is contained in Section 5.2.3.

Altering the radial-infall velocity at the outer boundary of the calculations has only a small affect on the relative accretion rates in most of the calculations, as observed by Artymowicz (1983). It does have large affect for very high-angular-momentum infall, however. This is discussed in detail in Section 5.2.3.

The main effect of increasing the size of the protostars is to reduce the extremes of the relative accretion rate; more material is accreted by the secondary relative to the primary for low-angular-momentum infall, and less is accreted by the secondary relative to the primary for high-angular-momentum infall. This is also discussed in detail in Section 5.2.3.

Of greatest significance to the evolution of the binary is the rate of change of the mass ratio - specifically when $\dot{q}/\dot{M}_{\rm b}$ changes sign (Figures 5.14b to 5.23b). Interestingly, for all mass ratios less than unity this seems to occur for approximately the same value of the cloud angular momentum of $j \approx 0.5 - 0.6$, with small-accretion-radii protostars (see also Figure 5.27). Below this value, the mass ratio decreases, above it increases.

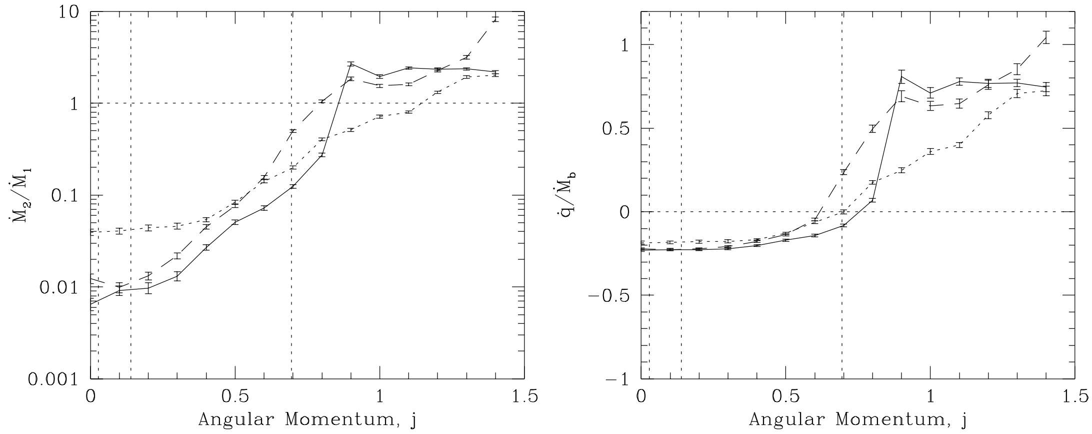

Figure 5.15: Effect of accretion on binary masses for a $q = 0.2$ binary. See Figure 5.14 for details.

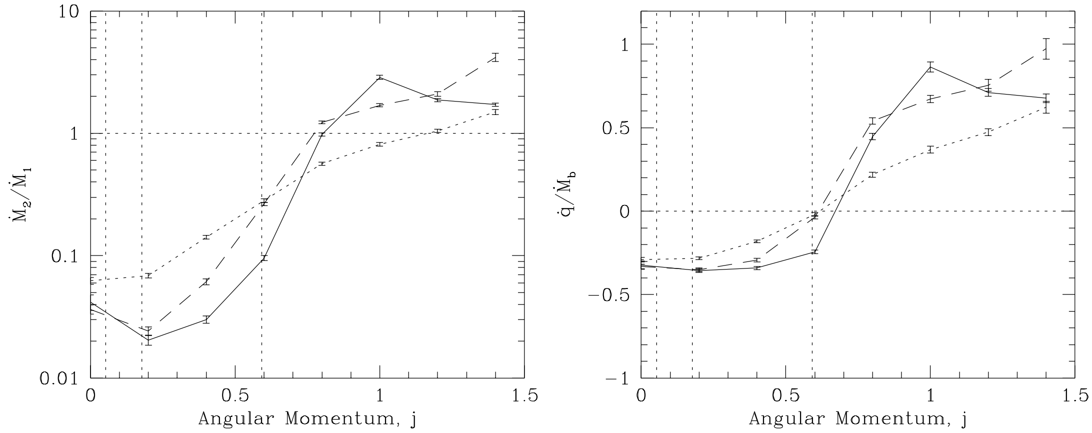

Figure 5.16: Effect of accretion on binary masses for a $q = 0.3$ binary. See Figure 5.14 for details.

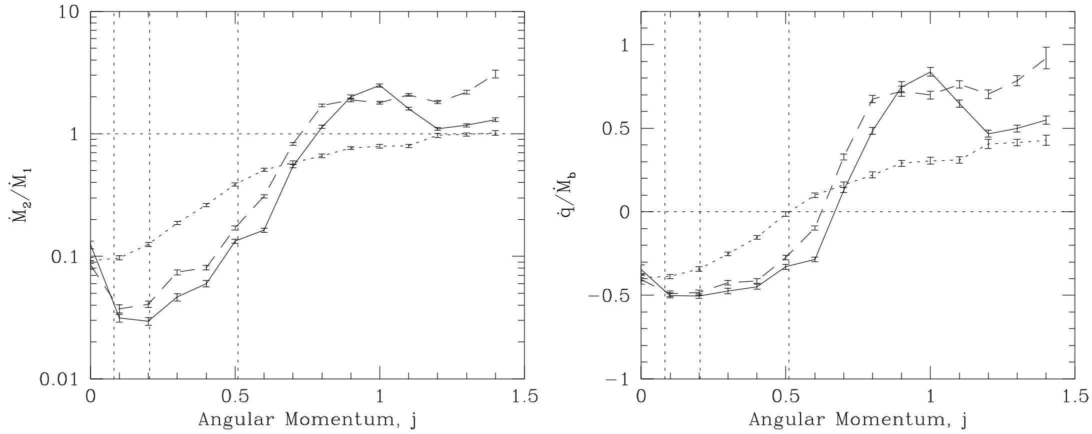

Figure 5.17: Effect of accretion on binary masses for a $q = 0.4$ binary. See Figure 5.14 for details.

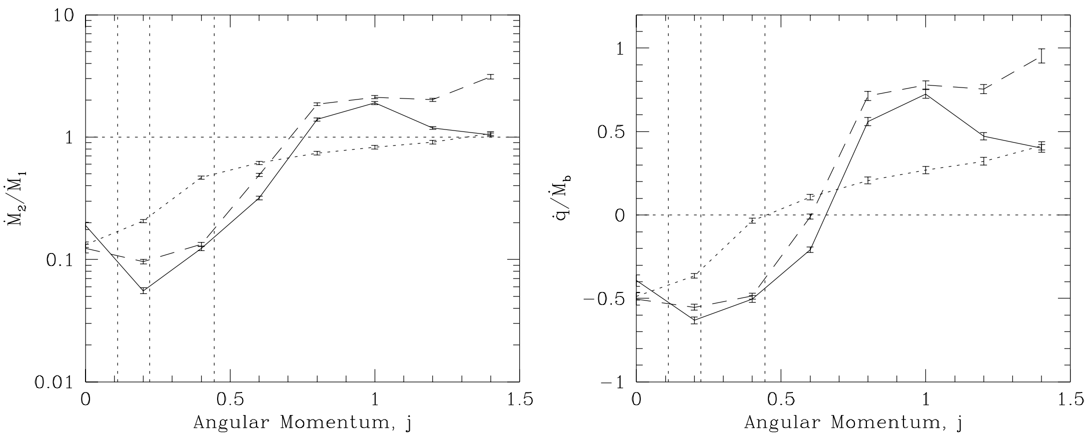

Figure 5.18: Effect of accretion on binary masses for a $q = 0.5$ binary. See Figure 5.14 for details.

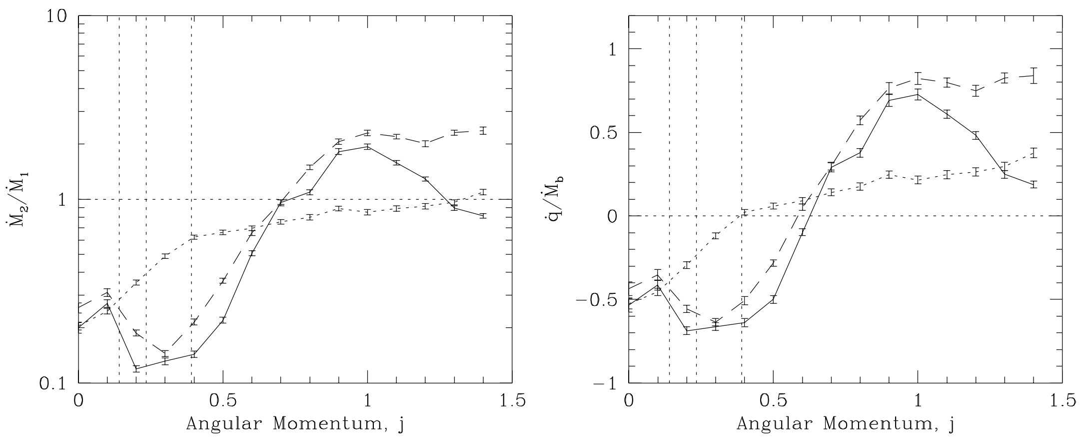

Figure 5.19: Effect of accretion on binary masses for a $q = 0.6$ binary. See Figure 5.14 for details.

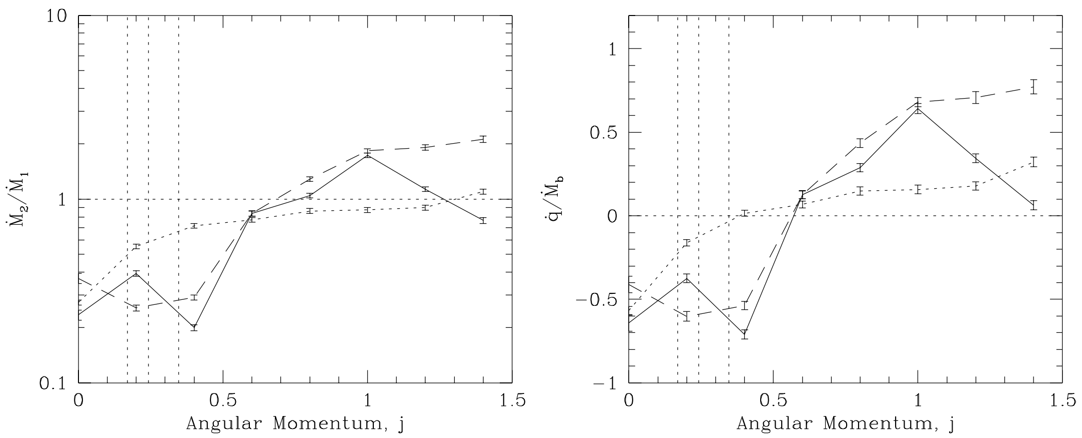

Figure 5.20: Effect of accretion on binary masses for a $q = 0.7$ binary. See Figure 5.14 for details.

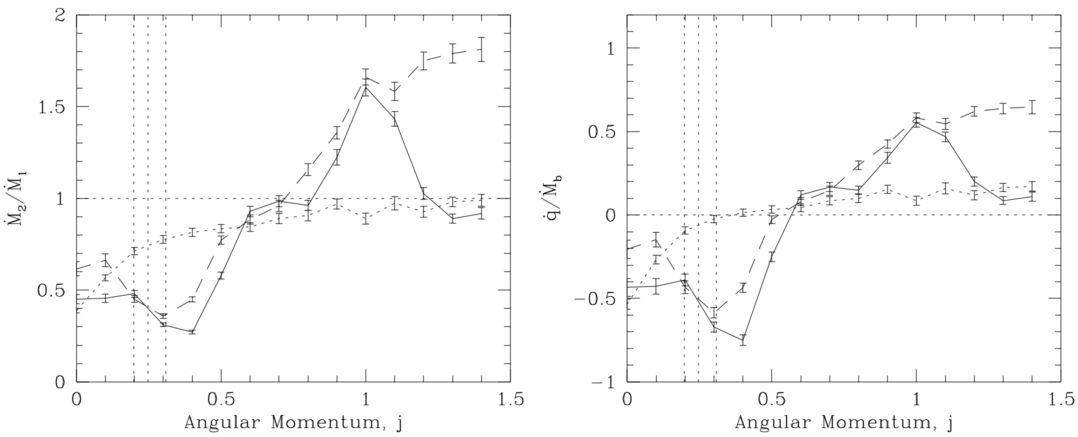

Figure 5.21: Effect of accretion on binary masses for a $q = 0.8$ binary. See Figure 5.14 for details.

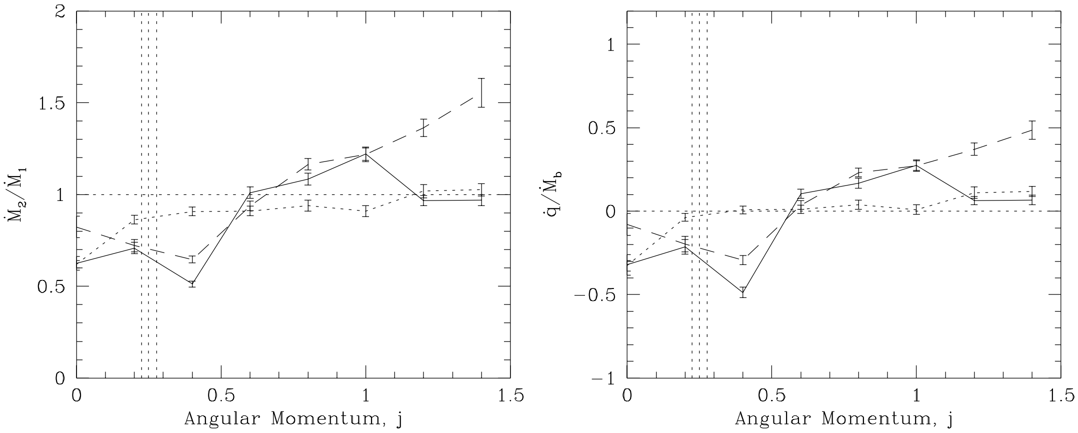

Figure 5.22: Effect of accretion on binary masses for a $q = 0.9$ binary. See Figure 5.14 for details.

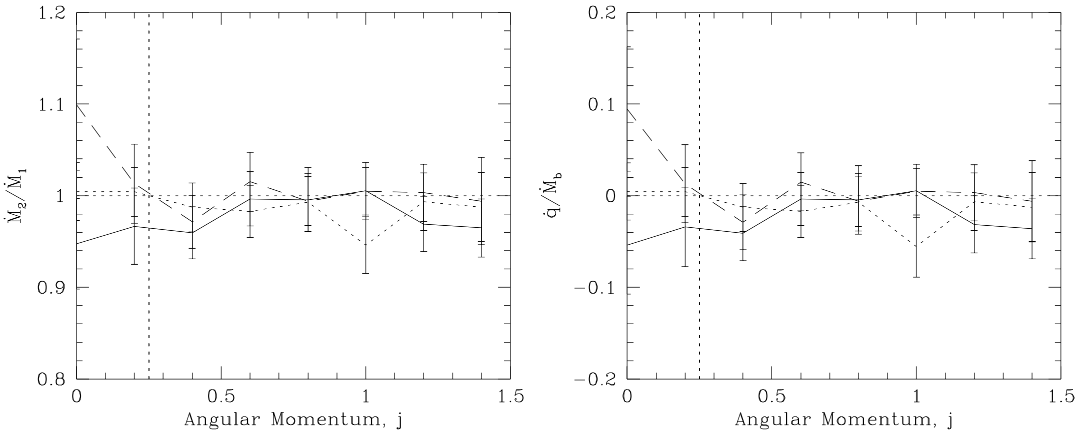

Figure 5.23: Effect of accretion on binary masses for a $q = 1.0$ binary. See Figure 5.14 for details.

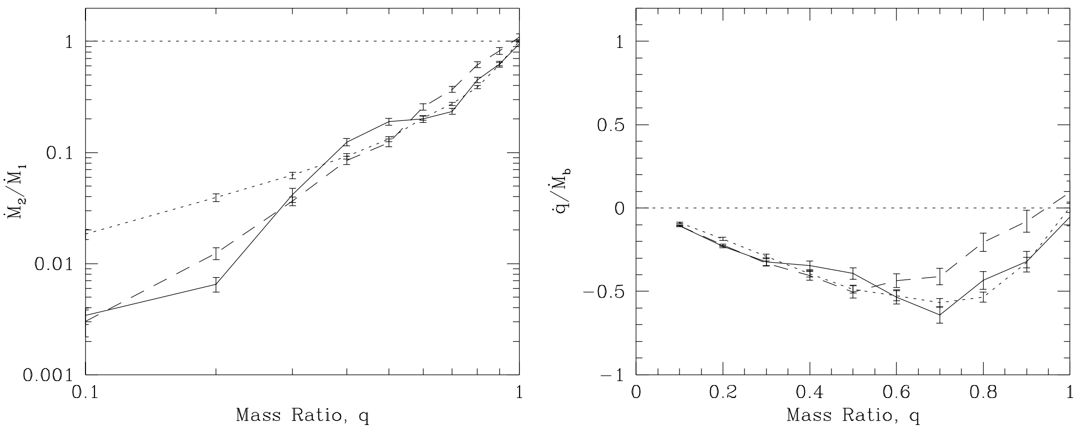

Figure 5.24: Effect of accretion of $j = 0.0$ angular momentum material on binary masses. Graph a) gives the relative accretion rate $\dot{M}_2/\dot{M}_1$ (left), and graph b) gives the rate of change of mass ratio per fractional mass accreted by the system $\dot{q}/\dot{M}_{\rm b}$ (right). The different curves are for: $r_{\rm acc} = 0.05D$ and $v_{\rm rad} = 1$ (solid); $r_{\rm acc} = 0.05D$ and $v_{\rm rad} = 0$ (dashed); $r_{\rm acc}$ equal to the mean-Roche-lobe radii and $v_{\rm rad} = 1$ (dotted). Estimated error bars are given.

The rate of change of $\dot{q}/\dot{M}_{\rm b}$ is also most rapid when $\dot{q}/\dot{M}_{\rm b} \approx 0$. This implies that under **constant**-angular-momentum infall, if the separation of the binary remains unchanged, the binary is either driven to a very low mass ratio (for $j \lesssim 0.5$) or equal masses (for $j \gtrsim 0.6$). In reality, of course, the angular momentum of the cloud material is not expected to remain constant, and the binary's separation may evolve. For protostars with mean-Roche-lobe sizes, the position of the change in sign of $\dot{q}/\dot{M}_{\rm b}$ does depend on the mass ratio - it occurs at lower j when the mass ratio is increased. This again implies that, in the absence of changes in the binary's separation and the angular momentum of the cloud material, a binary whose mass ratio is decreasing continues to have it decrease, and a binary whose mass ratio is increasing continues to have it increase. The empirical relation that $\dot{q}/\dot{M}_{\rm b} = 0$ when $j \approx j_2$ (for $q \neq 1$) fits the mean-Roche-lobe ballistic accretion results very well. For j below this value, the mass ratio decreases, above it increases. This approximate relation is not surprising because in the previous section we saw that for the mean-Roche-lobe accretion radii the accretion on to the secondary reaches a maximum when $j \approx j_2$.

Finally, as the mass ratio is decreased below $q = 0.3$, the magnitude of $\dot{q}/\dot{M}_{\rm b}$ decreases for low-angular-momentum infall (Figures 5.14 to 5.17 and Figures 5.24 to 5.26). This reflects the fact that as the mass ratio decreases, the mass of the primary must be increased more and more for the mass ratio to decrease by the same amount. This can also been determined by taking the limits of Equation 5.4. If all the mass falls on to the primary (low j), then $\dot{q}/\dot{M}_{\rm b} = -q(1+q)$, which tends to zero as $q \to 0$. If all the mass falls on to the secondary (high j), then $\dot{q}/\dot{M}_{\rm b} = (1+q)$. Note that in practice, this means that the maximum $\dot{q}/\dot{M}_{\rm b} \approx 1$, since as $q \to 1$, the relative accretion rate drops and $M_1/M_2 \neq 0$ (see Figure 5.31). For high mass ratios, the magnitude of $\dot{q}/\dot{M}_{\rm b}$

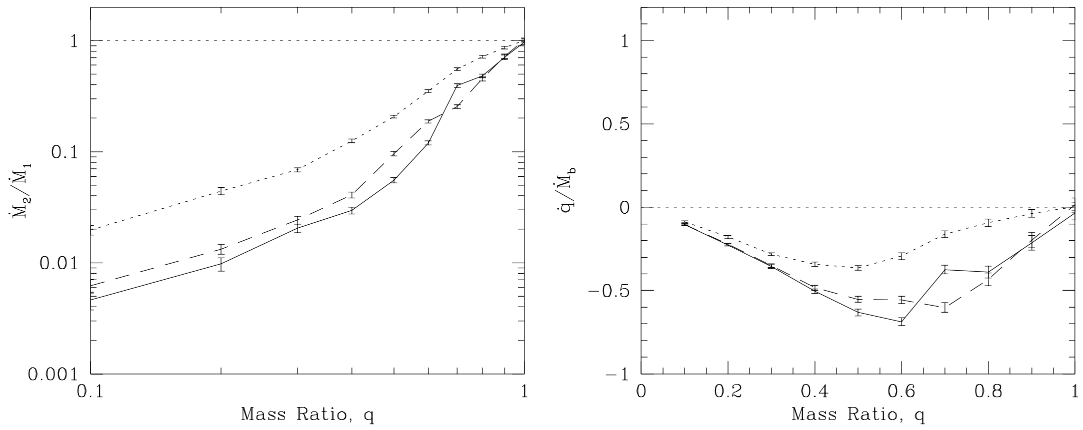

Figure 5.25: Effect of accretion of $j = 0.2$ angular momentum material on binary masses. See Figure 5.24 for details.

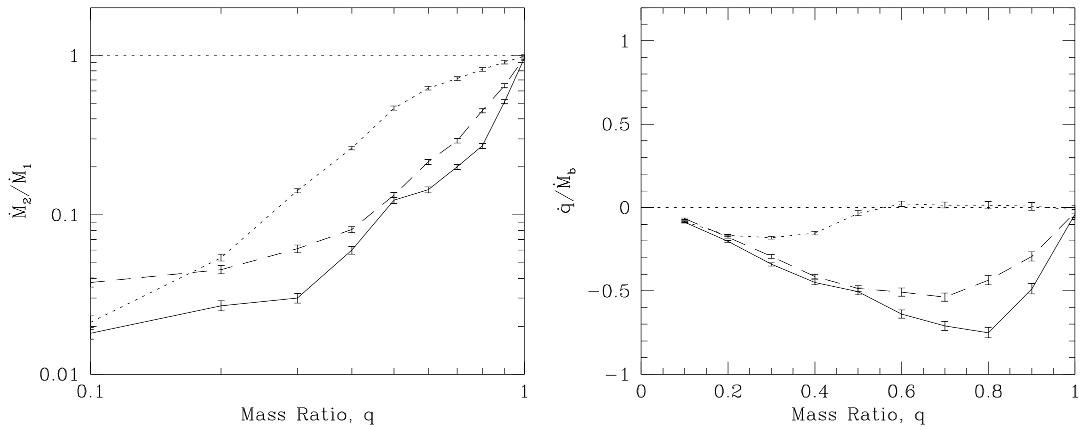

Figure 5.26: Effect of accretion of $j = 0.4$ angular momentum material on binary masses. See Figure 5.24 for details.

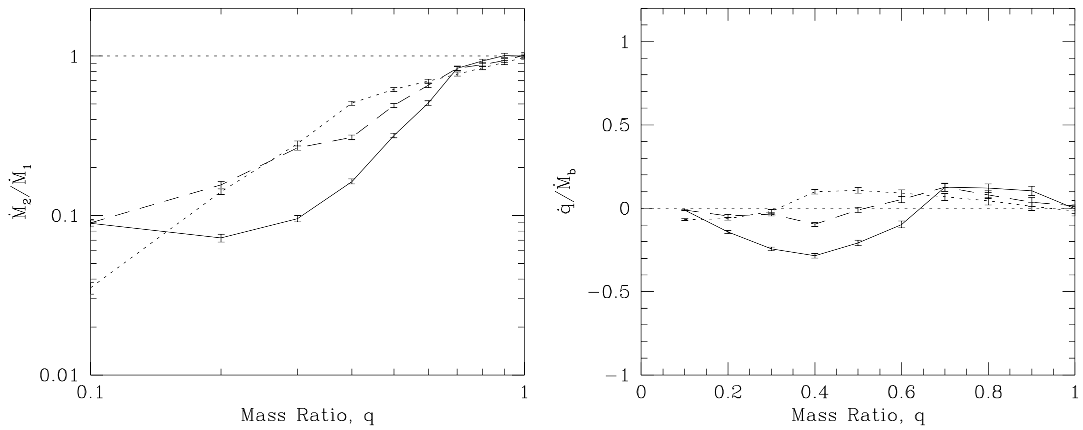

Figure 5.27: Effect of accretion of $j = 0.6$ angular momentum material on binary masses. See Figure 5.24 for details.

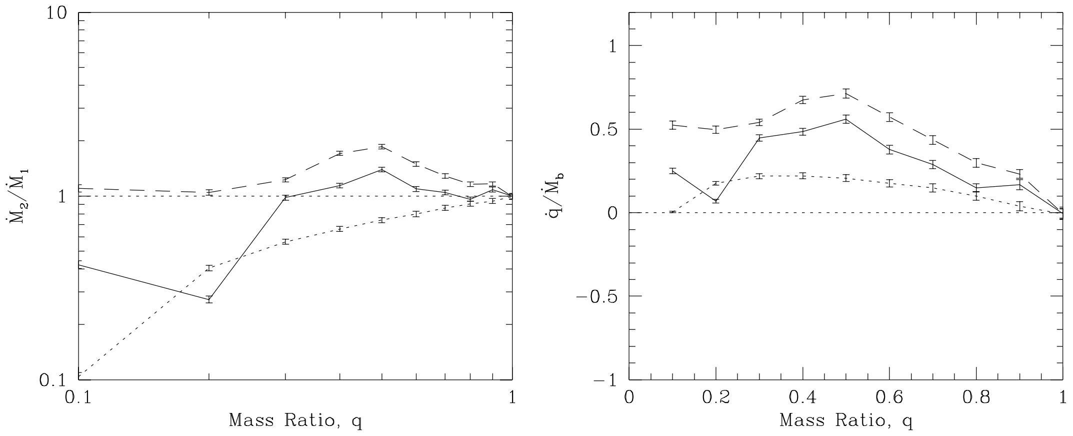

Figure 5.28: Effect of accretion of $j = 0.8$ angular momentum material on binary masses. See Figure 5.24 for details.

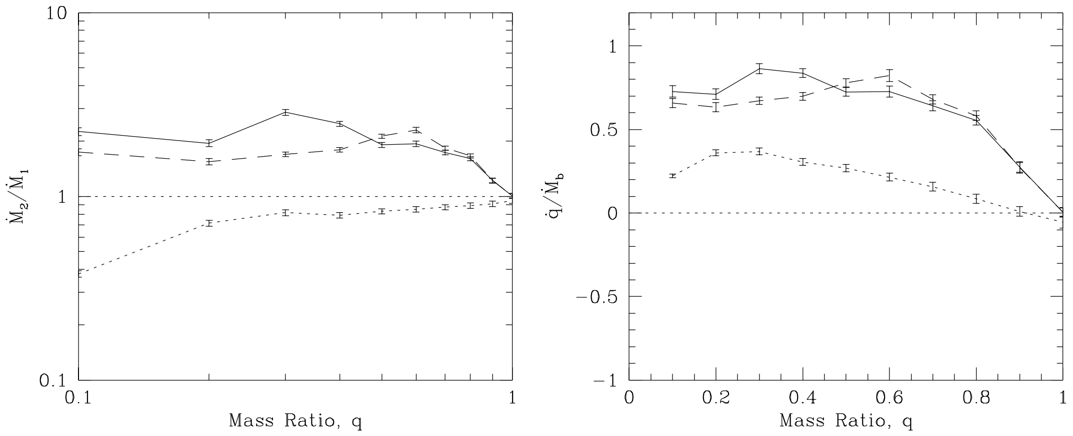

Figure 5.29: Effect of accretion of $j = 1.0$ angular momentum material on binary masses. See Figure 5.24 for details.

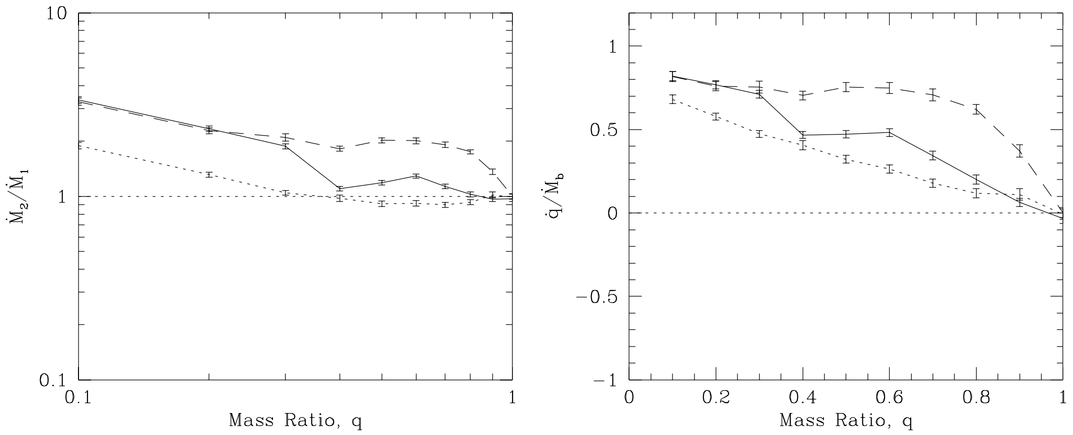

Figure 5.30: Effect of accretion of $j = 1.2$ angular momentum material on binary masses. See Figure 5.24 for details.

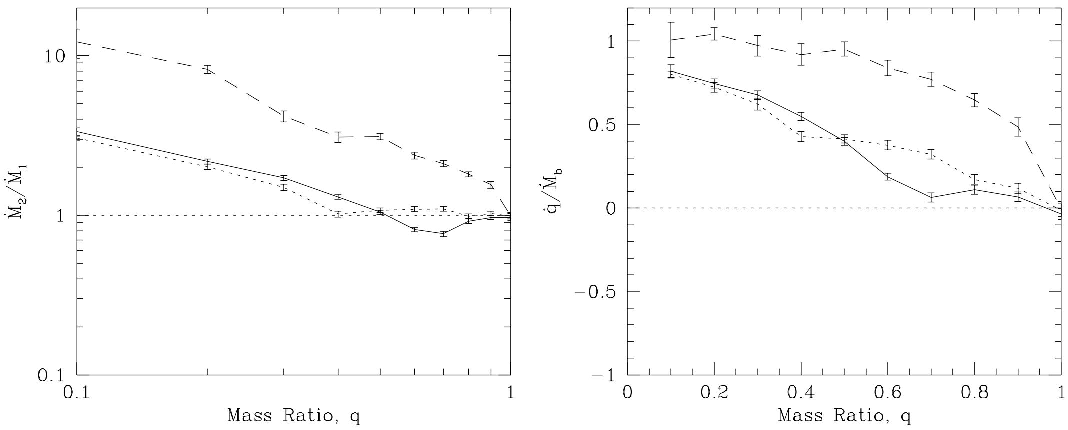

Figure 5.31: Effect of accretion of $j = 1.4$ angular momentum material on binary masses. See Figure 5.24 for details.

decreases for both positive and negative values, as the accretion becomes similar for the two protostars - and ultimately the same for $q = 1$ (Figures 5.20 to 5.23).

In summary, the qualitative results agree with Artymowicz (1983). The general dependencies on mass ratio, and the angular momentum of the cloud material are reproduced. However, Artymowicz studied mainly high mass ratios, and high-angular-momentum infall, so a much greater range of mass ratios and cloud angular momenta are studied here. This allows us to comment on the general use of the empirical relation Artymowicz gave for the relative accretion rate as a function of mass ratio (Equation 1.10). For high-angular-momentum accretion, of $V_{\rm tr} = 0.8$, Artymowicz found $c(V_{\rm tr}) = 3/2$ gave a good fit (see Section 1.4.2). It is not possible to correlate Artymowicz's cloud rotation parameter $V_{\rm tr}$ directly with the parameter j used here, but by comparison of Figure 1.5 with Figure 5.19, $V_{\rm tr} = 0.8$ is probably equivalent to $j \gtrsim 1.4$. Hence direct comparison with Artymowicz's Figure 1.5 can not be made. However, from Figures 5.24 to 5.31 a parameterisation such as Equation 1.10 could be used relatively successfully to represent the **global** behaviour of the relative accretion rate for $q \gtrsim 0.3$, although continuing this fit below $q = 0.3$ generally does not provide a good fit. The values of $c(j)$ thus obtained would increase from $c(j = 0) \approx -2.5$ up to $c(j = 1.4) \approx 0.5 - 1$. The problems with using such a parameterisation are first, that it depends critically on the assumed accretion radii of the protostars, and second, that for high-angular-momentum accretion it depends critically on radial-infall velocity $v_{\rm rad}$. Thus, although such parameterisations may be attempted, the values of $c(j)$ are very uncertain without performing gaseous accretion calculations.

5.2.3 Dependence on Accretion Radii and the Radial-Infall Velocity

The results given in Sections 5.2.1 and 5.2.2 were performed with accretion radii of either 1/20 the initial separation D, or the mean-Roche-lobe sizes of the protostars. In this section, the dependence of the results on the stellar accretion radius is investigated

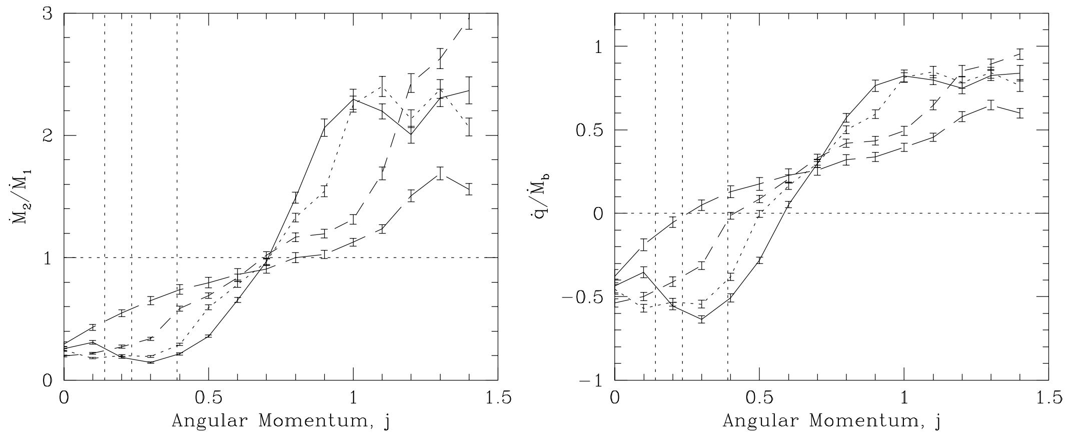

Figure 5.32: Effect of accretion on binary masses for a $q = 0.6$ binary as a function of cloud angular momentum j, and with zero-radial-infall velocity at the outer boundary ($v_{\rm rad} = 0$). Different protostellar accretion radii of $r_{\rm acc} = 0.05D$ (solid), $r_{\rm acc} = 0.10D$ (dotted), $r_{\rm acc} = 0.20D$ (short-dashed), and $r_{\rm acc} = 0.40D$ (long-dashed) are used in each case. Graph a) gives the relative accretion rate $\dot{M}_2/\dot{M}_1$. Graph b) gives the rate of change of mass ratio per unit mass accreted by the system $q/\dot{M}_{\rm b}$. Estimated error bars are given. The vertical lines give the specific orbital angular momentum of the primary (left), the binary (middle), and the secondary (right).

in more detail. The affect of varying the radial-infall velocity is also discussed.

Artymowicz (1983) varied his protostellar radii $R_{\rm i}$, as

$$R_{\rm i} = R_0 M_{\rm i}^n \tag{5.10}$$

where $M_{\rm i}$ are the masses of the stars, and n was varied between $-1/3 < n < 1/3$. Artymowicz found his results were not significantly dependent on the value of n. Unfortunately, it is not stated what R_0 was in terms of the binary separation, or if this was changed! In the following analysis, the value of n is set to zero for all simulations, and only the value of $R_0 = r_{\rm acc}$ is varied.

To determine the dependence on protostellar accretion radius, an intermediate mass ratio of $q = 0.6$ is chosen to allow comparison to the results of Artymowicz (1983). Using a mass ratio of $q = 0.6$, 90 additional simulations were performed varying the cloud's angular momentum from $j = 0$ to $j = 1.4$ as before, and for each of these varying the stellar accretion radius in multiples of two from $r_{\rm acc} = 0.05D$ to $r_{\rm acc} = 0.40D$. Calculations were also performed with $v_{\rm rad} = 0$ and $v_{\rm rad} = 1$ to examine the dependence on the radial-infall velocity. The results are presented in Figures 5.32 and 5.33.

The relative accretion rates, depend greatly on the accretion radius. Generally, the range of the relative accretion rates decreases with increasing accretion radius with the results tending toward unity for all cloud angular momenta. For $r_{\rm acc} = 0.40D$, the relative accretion rates are constrained to between $0.3 \lesssim \dot{M}_2/\dot{M}_1 \lesssim 1.7$ for all values of j. Note that the value of j for which the relative accretion rate is unity is **independent** of the accretion radius at $j \approx 0.7$. In Section 5.2.2 it was noted that for $r_{\rm acc} = 0.05D$,

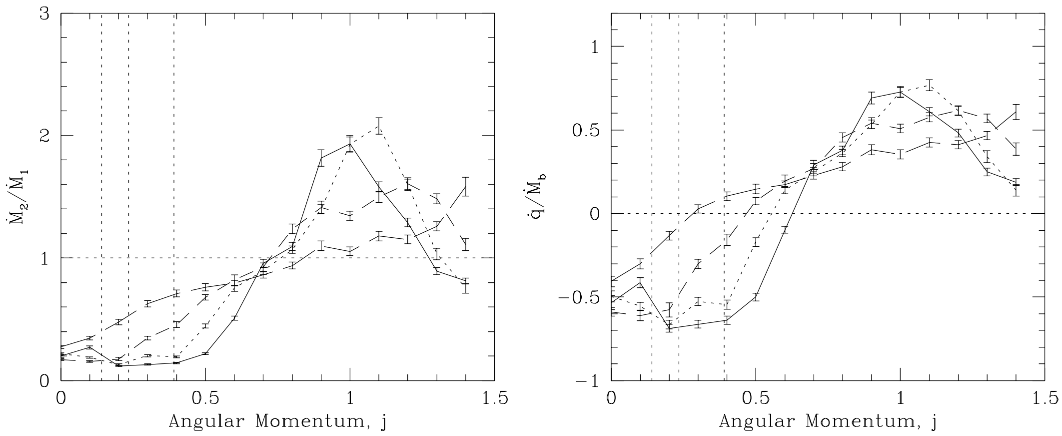

Figure 5.33: Effect of accretion on binary masses for a $q = 0.6$ binary as a function of cloud angular momentum j, and with a radial-infall velocity at the outer boundary of $v_{\rm rad} = 1$. See Figure 5.32 for details.

the value of j for which the relative accretion rate is unity is almost independent of mass ratio as well. However, these relations are true only if the two protostars have the same sizes - when the mean-Roche-lobe sizes are used, they disappear. For $q > 0.5$, the secondary appears never to accrete significantly more than the primary, even for angular momentum as high as $j = 1.4$ (Figures 5.18 to 5.23). This is because the secondary, with its smaller size, accretes less so that j must be larger to give a relative accretion rate of unity.

Comparing the results to those of Artymowicz in Figure 1.4, it is found that a good match is only attained for a large value of $r_{\rm acc}$. For small $r_{\rm acc}$, the relative accretion rate changes rapidly for intermediate values of j. Artymowicz's results, however, give a 'plateau' at intermediate cloud angular momenta of a relative accretion rate near unity. This is only reproduced in Figures 5.32 and 5.33 for $r_{\rm acc} \approx 0.40D$. Thus, Artymowicz must have used a large protostellar size in comparison with the binary separation. Since he was mainly considering accretion on to close binaries, this may not be a bad approximation, especially if during their formation the stars are surrounded by large discs. For wide binaries, however, the appropriate protostellar size is a matter of debate. Comparison with the gaseous accretion results in Chapter 6 are needed to resolve this issue.

For the rate of change of the mass ratio (Figures 5.32b and 5.33b), the effect of changing the accretion radii is the same as that for the relative accretion rate - the range of $\dot{q}/\dot{M}_{\rm b}$ decreases toward zero as the accretion radius is increased. Also, the value of j for which $\dot{q} = 0$ decreases with increasing $r_{\rm acc}$. For the largest accretion radius it occurs when j is equal to the specific angular momentum of the binary. This shifting toward lower j should only be important for high mass ratios in reality, however, as for small mass ratios the secondary's size should be limited to its Roche-lobe size. This is apparent in Figures 5.14 to 5.23 where only high mass ratios have $\dot{q} = 0$ at low j.

The results given in Sections 5.2.1 and 5.2.2 should be viewed as giving the extremes of the relative accretion rate: if the appropriate sizes of the protostars are small, the ballistic results with $r_{\rm acc} = 0.05D$ will be closest to the true behaviour of the system, while the largest possible size of the protostars and/or their discs should be given by the mean-Roche-lobe-sized protostars. If the appropriate sizes are somewhere in between, the results discussed in this section will give an idea of correct relative accretion rates.

Finally, changing the radial-infall velocity at the outer boundary has only a small effect for $j \lesssim 1$ for all accretion radii (Figures 5.32 and 5.33). Artymowicz also stated his results were independence of the radial-infall velocity. This is not the case for $j \gtrsim 1$, however. With increased radial-infall velocity, the relative accretion rate and $\dot{q}/\dot{M}_{\rm b}$ decrease. As discussed in section 5.2.2 this is because the particles are on more elliptical trajectories, with smaller periastron distances, and thus are more likely to be accreted by the primary. With dissipative accretion, the relative accretion rate may be expected to be very high for $j \gtrsim 1$ since the gas will dissipate much of its radial-infall velocity in the formation of a circumbinary disc.

The effect of the radial-infall velocity does depend on the sizes of the protostars. For large protostars, the radial-infall velocity has little effect on the results as the secondary intercepts much of the infalling material before it gets to the primary regardless. Thus, if the sizes of the protostars do depend on their masses, such as their Roche-lobe sizes, the radial velocity may affect the results more for low mass ratios because the secondary will be smaller. With gaseous accretion this effect may be offset, however, because the accretion will be from a circumbinary disc with a low radial-infall velocity regardless of the initial value.

5.3 Effects of Ballistic Accretion on Binary Separation

Accretion on to a binary affects not only the masses, but also the orbital elements of the system. The effect on the separation of the binary is investigated using results from the simulations presented in Section 5.2.

5.3.1 Effects Due to Accretion and Particle Losses

The effect of ballistic accretion on the semi-major axis separation of a binary is given in Figures 5.34 to 5.43. The rate of change of separation per unit total mass accreted $\dot{a}/\dot{M}_{\rm b}$ is given as a function of the angular momentum of the cloud. If the change in separation was due only to the accretion of particles by the binary, then $\dot{a}/\dot{M}_{\rm b}$ would be sufficient to give the change in separation for a known accretion rate on to the binary. However, with ballistic accretion, not all particles that enter the simulation are accreted. Many, as discussed previously, fall toward the binary, gain angular momentum and energy, and then are expelled from the system to the outer boundary of the calculation. When these particles are removed, there is a net loss of angular momentum from the system, and the binary loses the orbital angular momentum

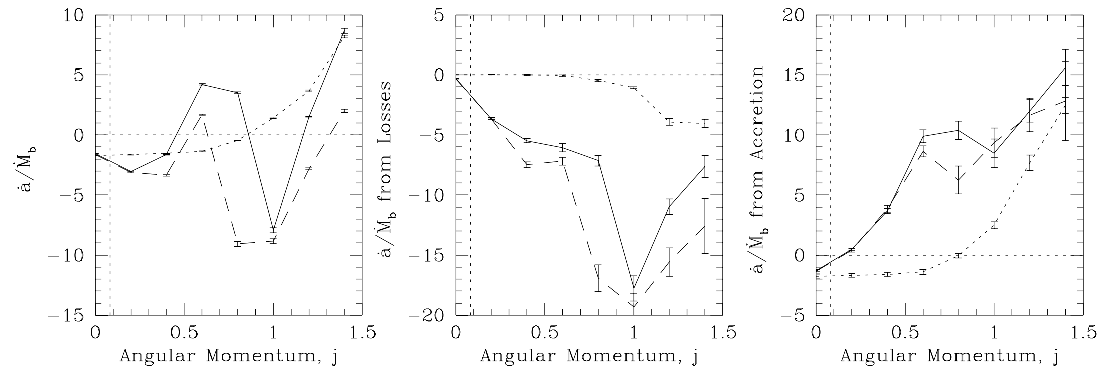

Figure 5.34: Effect of accretion on binary separation for a $q = 0.1$ binary. The graphs are plotted as a function of the angular momentum j of the infalling cloud. Graph a) gives the rate of change of separation per unit mass accreted by the binary $\dot{a}/\dot{M}_{\rm b}$ (left). Graph b) gives the contribution to $\dot{a}/\dot{M}_{\rm b}$ due only to the loss of angular momentum from the binary via transfer to ballistic particles lost from the simulation (centre). Graph c) gives $\dot{a}/\dot{M}_{\rm b}$ due to the accretion of particles only (right). The different curves are for: $r_{\rm acc} = 0.05D$ and $v_{\rm rad} = 1$ (solid); $r_{\rm acc} = 0.05D$ and $v_{\rm rad} = 0$ (dashed); $r_{\rm acc}$ equal to the mean-Roche-lobe radii and $v_{\rm rad} = 1$ (dotted). Estimated error bars are given. The vertical lines give the specific orbital angular momentum of the binary.

that the particle gained. This loss of orbital angular momentum decreases the separation. The effects of the loss of orbital angular momentum of the binary due to gravitational torques acting on particles that are expelled, and the effects of accretion on the binary's separation, are given separately in Figures 5.34 to 5.43. These two separate contributions can be calculated by differentiating the equation for the orbital angular momentum of the binary about its centre of mass

$$L = \sqrt{GM_{\rm b}^3 a}\frac{q}{(1+q)^2} \tag{5.11}$$

with respect to time to give

$$\frac{{\rm d}a}{{\rm d}t} = \frac{2(1+q)^2}{q}\sqrt{\frac{a}{GM_{\rm b}^3}}\frac{{\rm d}L}{{\rm d}t} - \frac{3a}{M_{\rm b}}\frac{{\rm d}M_{\rm b}}{{\rm d}t} - \frac{2a(1-q)}{q(1+q)}\frac{{\rm d}q}{{\rm d}t}. \tag{5.12}$$

The rate of loss of angular momentum from the system due to the removing of particles at the outer boundary then gives the effect on the separation from this loss. It can be subtracted to leave the effect on separation simply due to the accretion. As a check on this, $\dot{a}$ due to accretion can also be calculated from the amount of orbital angular momentum accreted by the binary, and $\dot{M}_{\rm b}$ and $\dot{q}$ which are already known. The differences in these two methods of extracting the two contributions to $\dot{a}$ give the error estimates.

In Chapter 6, with gaseous accretion, particles not immediately accreted will interact with other particles via viscosity, dissipating excess energy. They will not escape and carry off angular momentum and energy from the binary. Hence, the effects of the ballistic accretion on separation due to accretion only are expected to match the gaseous

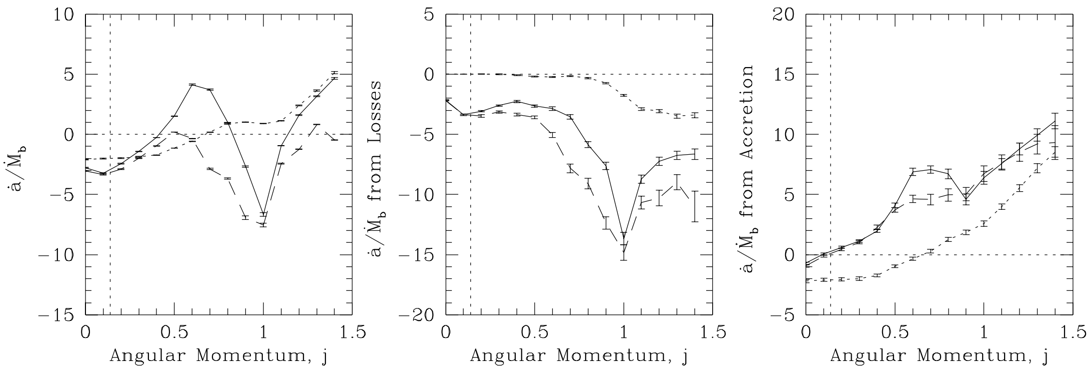

Figure 5.35: Effect of accretion on binary separation for a $q = 0.2$ binary. See Figure 5.34 for explanation.

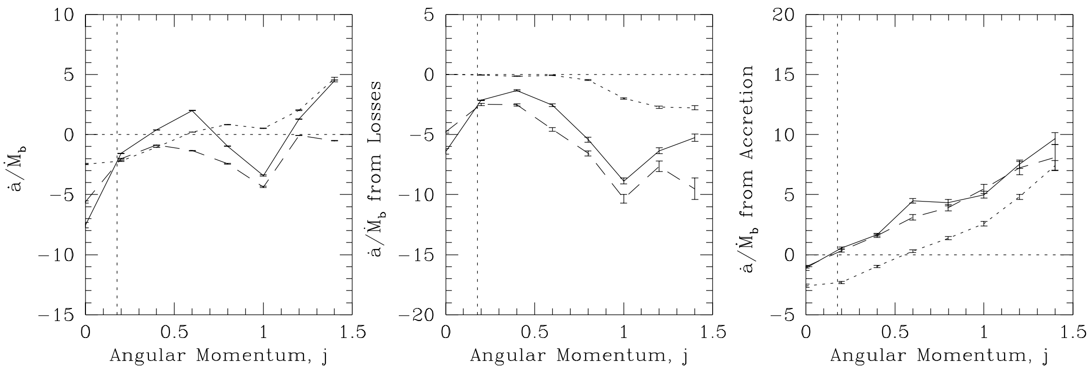

Figure 5.36: Effect of accretion on binary separation for a $q = 0.3$ binary. See Figure 5.34 for explanation.

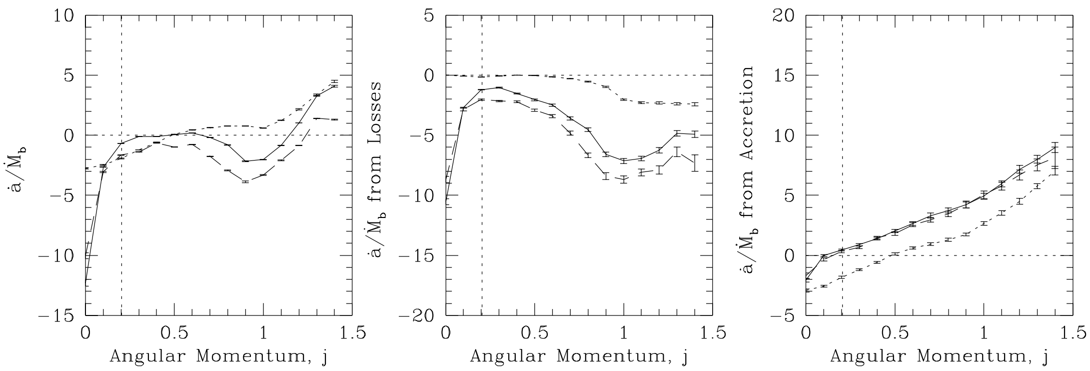

Figure 5.37: Effect of accretion on binary separation for a $q = 0.4$ binary. See Figure 5.34 for explanation.

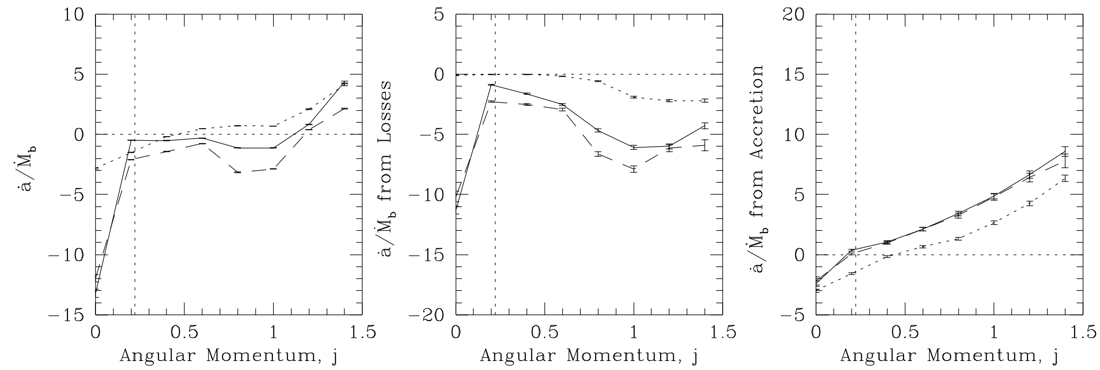

Figure 5.38: Effect of accretion on binary separation for a $q = 0.5$ binary. See Figure 5.34 for explanation.

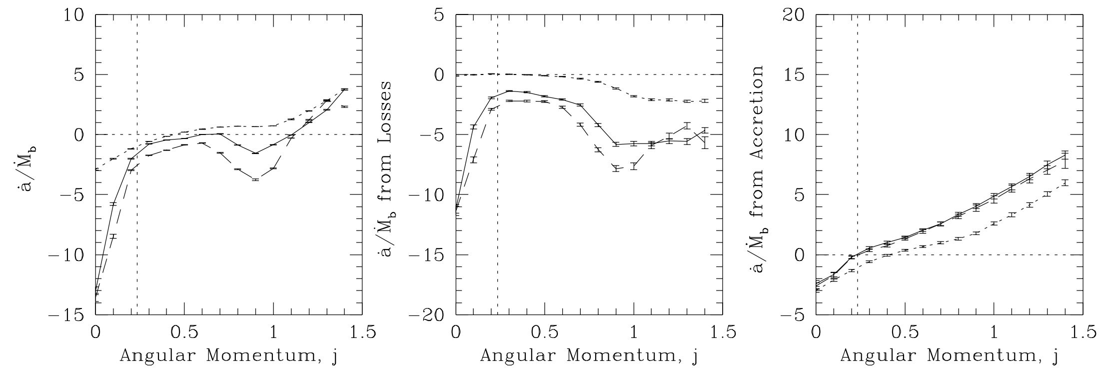

Figure 5.39: Effect of accretion on binary separation for a $q = 0.6$ binary. See Figure 5.34 for explanation.

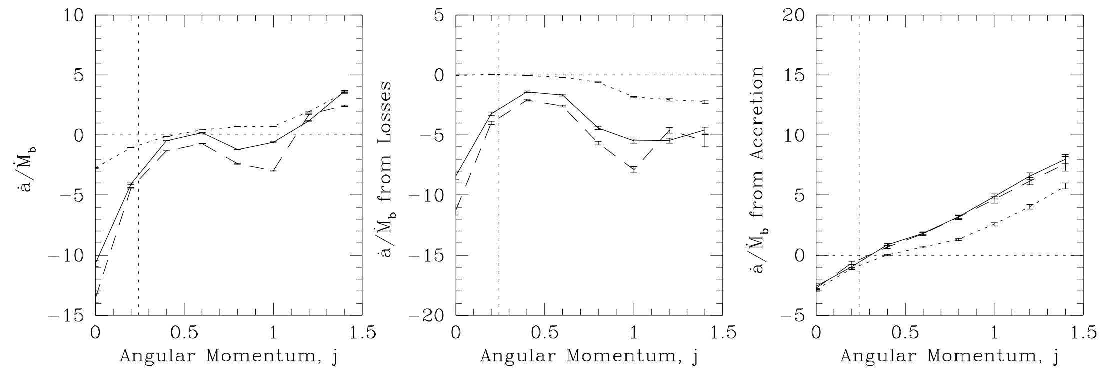

Figure 5.40: Effect of accretion on binary separation for a $q = 0.7$ binary. See Figure 5.34 for explanation.

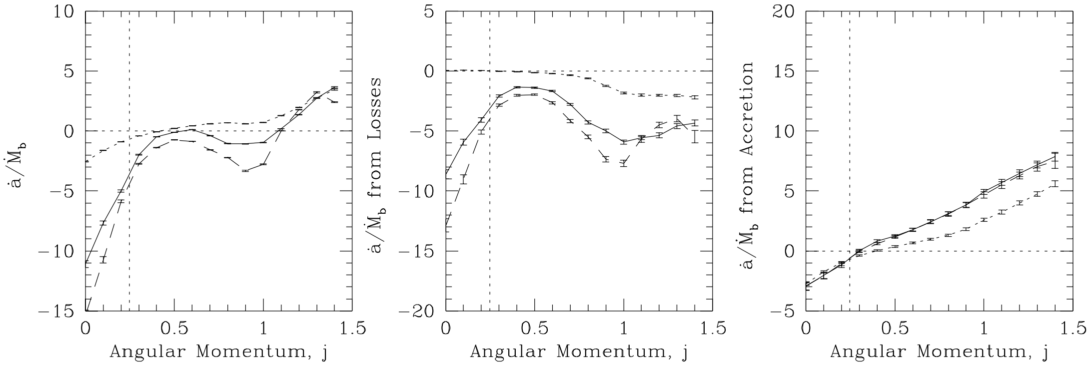

Figure 5.41: Effect of accretion on binary separation for a $q = 0.8$ binary. See Figure 5.34 for explanation.

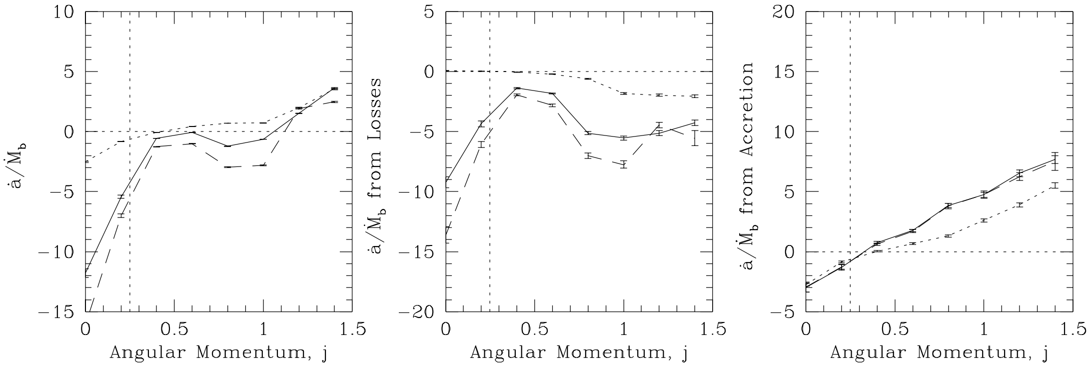

Figure 5.42: Effect of accretion on binary separation for a $q = 0.9$ binary. See Figure 5.34 for explanation.

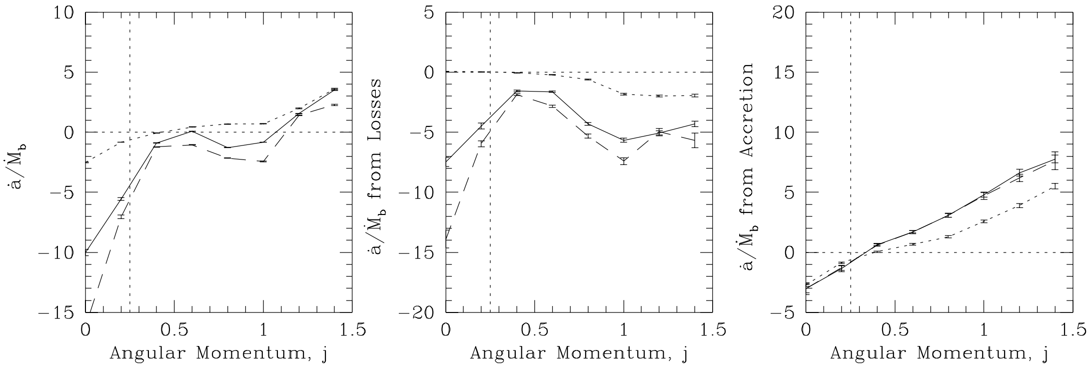

Figure 5.43: Effect of accretion on binary separation for a $q = 1.0$ binary. See Figure 5.34 for explanation.

accretion results the best. The effect due to the loss of particles is purely an artifact of using ballistic particles.

Consider the total effect of ballistic accretion on the binary, for the calculations with $r_{\rm acc} = 0.05D$ (Figures 5.34a to 5.43a). In most cases, the separation of the binary is decreasing. Only for the very highest j does it consistently increase. Also, in most cases, there are two local minima in $\dot{a}/\dot{M}_{\rm b}$. The first occurs at $j \approx 0$. The second occurs at $j \approx 1$. From Figures 5.34b to 5.43b these minima are given predominantly by the angular momentum lost by the binary to the ballistic particles that are expelled. For the mean-Roche-lobe-sized protostars, this loss of angular momentum to expelled particles is much lower. Only for $j \gtrsim 0.8$ does it have much of an effect. This is because a greater fraction of the infalling particles are accreted for the larger-accretion-radii calculations, and particles are accreted farther from the protostars so that close encounters with the protostars which transfer a lot of angular momentum to the particles cannot occur. The effect due to losses grows for $j \gtrsim 0.8$ because the fraction of particles that are expelled increases.

Eliminating the effect from particle losses, we are left with Figures 5.34c to 5.43c, giving solely the effect of accreted particles on the binary. The most striking observation is that, generally, the graphs of $\dot{a}/\dot{M}_{\rm b}$ are monotonically increasing with j. Only the small-accretion-radii calculations with $q \lesssim 0.3$ break with this trend. This behaviour is expected, as the accretion of higher-angular-momentum material should increase the specific orbital angular momentum of the binary more, and thus its separation. Furthermore, for the small-accretion-radii calculations, the change from decreasing to increasing the separation occurs when the specific angular momentum of the infalling cloud material equals the specific angular momentum of the binary

$$j = j_{\rm b} = \sqrt{GM_{\rm b}a}\frac{q}{(1+q)^2}, \tag{5.13}$$

as is expected. With accretion radii equal to the mean-Roche-lobe sizes, this does not happen. Instead, there is always a region where $j > j_{\rm b}$, and yet the binary's separation decreases. Also, in all cases, $\dot{a}/\dot{M}_{\rm b}$ is less for the large-accretion-radii protostars than the small. This effect is also demonstrated in Figures 5.44 and 5.45 which give the effect of accretion on the separation of a $q = 0.6$ binary with accretion radii increasing in multiples of two from $r_{\rm acc} = 0.05D$ to $r_{\rm acc} = 0.40D$. As the accretion radius is increased, the rate of change of separation due to accretion decreases in nearly all cases. This dependence on the accretion radii of the protostars is because a particle that is accreted at a larger radius from a protostar has more angular momentum relative to the protostar than for accretion at a smaller radius (see also Section 5.4).

Changing the initial radial-infall velocity of the cloud has negligible effect on the rate of change of separation, once the effects of particle losses have been removed, for $q \gtrsim 0.3$ (Figures 5.34 to 5.43 and also Figures 5.44 and 5.45). This is because for high mass ratios it is the specific angular momentum of the accreted material more than the rate of change of mass ratio that affects the separation. For low mass ratios, $\dot{q}$ does affect the

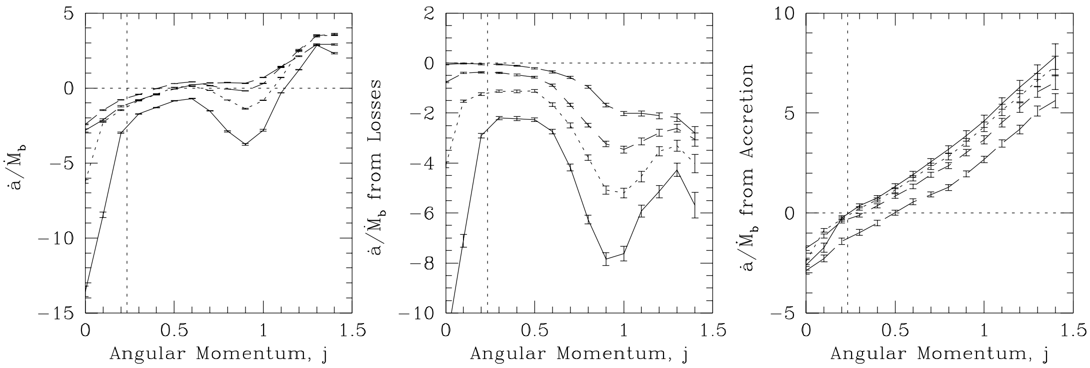

Figure 5.44: Effect of accretion on binary separation for a $q = 0.6$ binary as a function of cloud angular momentum j, and with zero radial-infall velocity at the outer boundary ($v_{\rm rad} = 0$). Different protostellar accretion radii of $r_{\rm acc} = 0.05D$ (solid), $r_{\rm acc} = 0.10D$ (dotted), $r_{\rm acc} = 0.20D$ (short-dashed), and $r_{\rm acc} = 0.40D$ (long-dashed) are used in each case. Graph a) gives the relative accretion rate $\dot{M}_2/\dot{M}_1$ (left). Graph b) gives the rate of change of mass ratio per unit mass accreted by the system $q/\dot{M}_{\rm b}$ (right). Estimated error bars are given. The vertical lines give the specific orbital angular momentum of the binary.

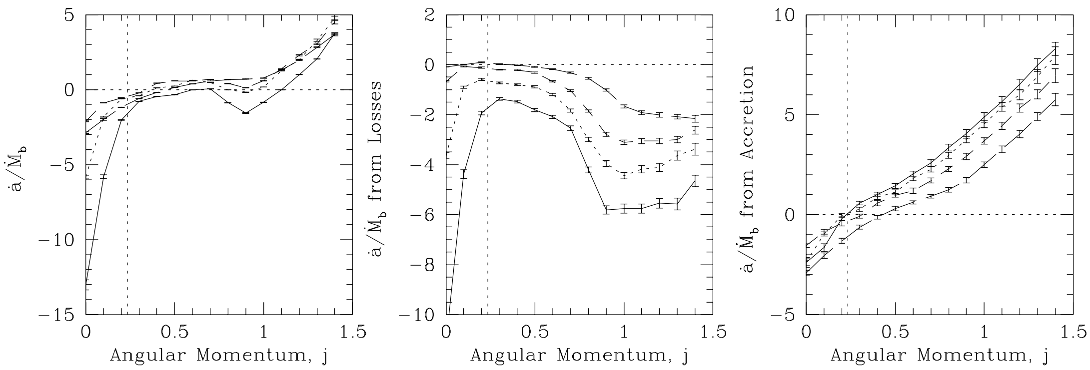

Figure 5.45: Effect of accretion on binary separation for a $q = 0.6$ binary as a function of cloud angular momentum j, and a radial velocity at the outer boundary of $v_{\rm rad} = 1$. See Figure 5.44 for explanation.

results (see the third term in Equation 5.12), and hence so does the radial-infall velocity upon which $\dot{q}$ depends in the range $0.6 \lesssim j \lesssim 0.8$ (c.f. Figures 5.34 to 5.36).

Comparing the results from Figures 5.44 and 5.45 to Artymowicz's results for the rate of change of separation of a $q = 0.6$ binary (Figure 1.6), we find the closest match to his results from Figure 5.45a, with $r_{\rm acc} = 0.40$ and $v_{\rm rad} = 1$. This again confirms the conclusion in Section 5.2.3, that Artymowicz used very large accretion radii for his calculations. Judging from the form of the curves, he also may not have attempted to take account of the distinction between changes in the separation due to losses from expelled particles (which are not physical), and changes due to accretion of particles.

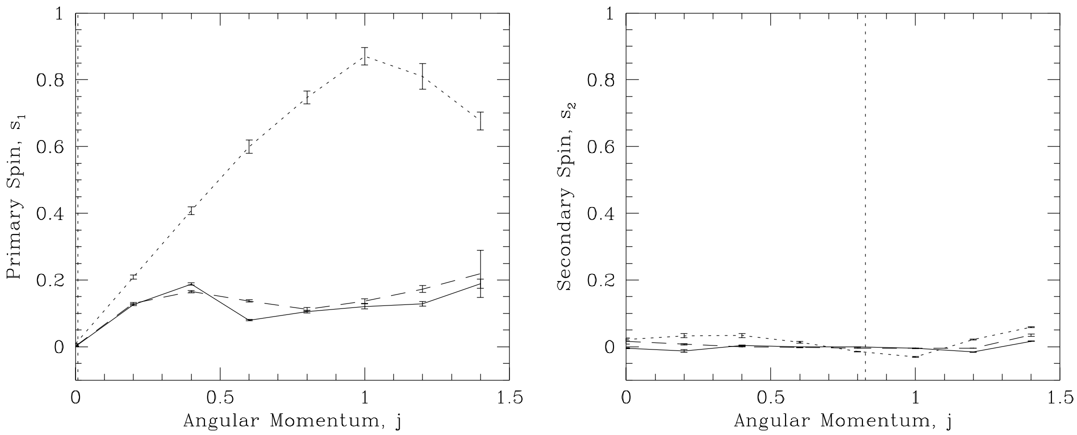

Figure 5.46: The specific spin angular momentum of the material accreted by each of the components of a $q = 0.1$ binary. The graphs are plotted as a function of the specific angular momentum j of the infalling cloud. The specific spin accreted by the primary s_1 (left), and the specific spin accreted by the secondary s_2 (right) are given. The different curves are for: $r_{\rm acc} = 0.05D$ and $v_{\rm rad} = 1$ (solid); $r_{\rm acc} = 0.05D$ and $v_{\rm rad} = 0$ (dashed); $r_{\rm acc}$ equal to the mean-Roche-lobe radii and $v_{\rm rad} = 1$ (dotted). Estimated error bars are given. The vertical lines give the specific orbital angular momentum of the primary (left) and secondary (right).

When this is taken into account, the change in separation under accretion is even more rapid than he found for $j \gtrsim 0.5$.

For gaseous accretion, the general increase of $\dot{a}/\dot{M}_{\rm b}$ with increasing angular momentum of the cloud should be maintained. The large and small-accretion-radii ballistic results differ quantitatively, however, so gaseous calculations are needed to determine the true effective sizes of the protostars. Also, with gaseous accretion, a circumbinary disc will form for high-angular-momentum infall. This will affect the binary differently to ballistic accretion. For example, when accreting from a circumbinary disc, the radial-infall velocity of the gas will be lower than for ballistic accretion. Also, the binary may lose angular momentum to the circumbinary disc via gravitational torques (Section 1.4.2).

5.4 Effects of Ballistic Accretion on Protostellar Spin

In the previous section, we found the rate of change of the binary's separation depends on the relative amounts of orbital and spin angular momentum accreted by the protostars. The larger the protostellar sizes, the more of the cloud's angular momentum is converted to spin angular momentum of the protostars and the less orbital angular momentum is given to the binary. This results in a lower rate of change of separation for a binary with larger-accretion-radii protostars.

In Figures 5.46 to 5.55 the specific spin angular momentum of the material accreted by the protostars is presented as a function of the cloud angular momentum for different mass ratio binaries. Indeed, the protostars with mean-Roche-lobe-sized accretion radii

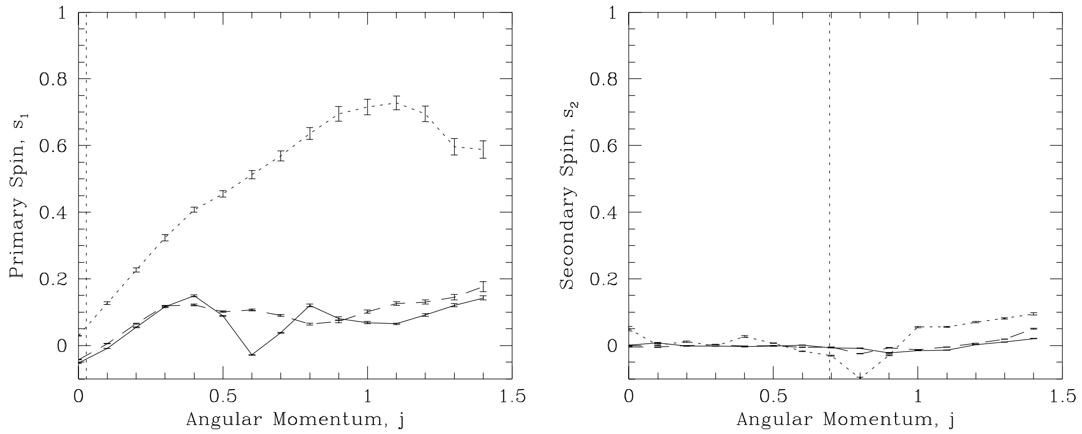

Figure 5.47: The specific spin angular momentum accreted by each of the binary components of a $q = 0.2$ binary. See Figure 5.46 for explanation.

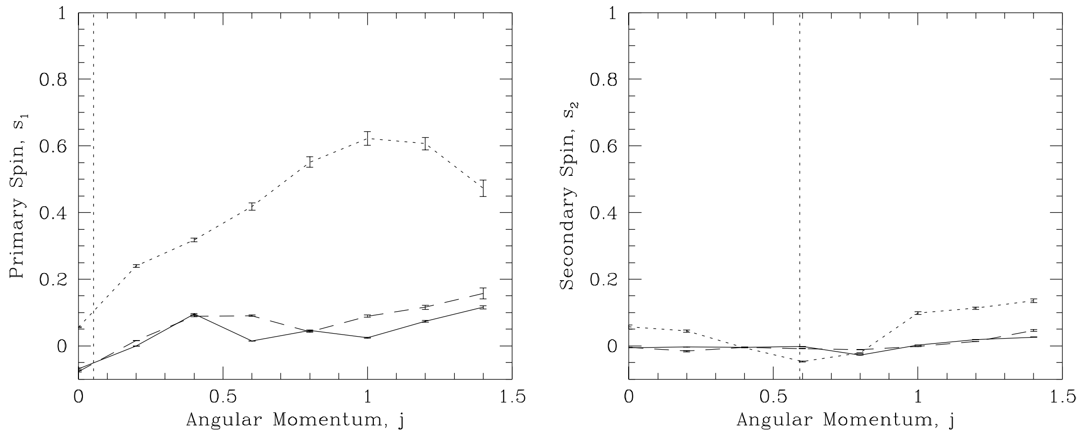

Figure 5.48: The specific spin angular momentum accreted by each of the binary components of a $q = 0.3$ binary. See Figure 5.46 for explanation.

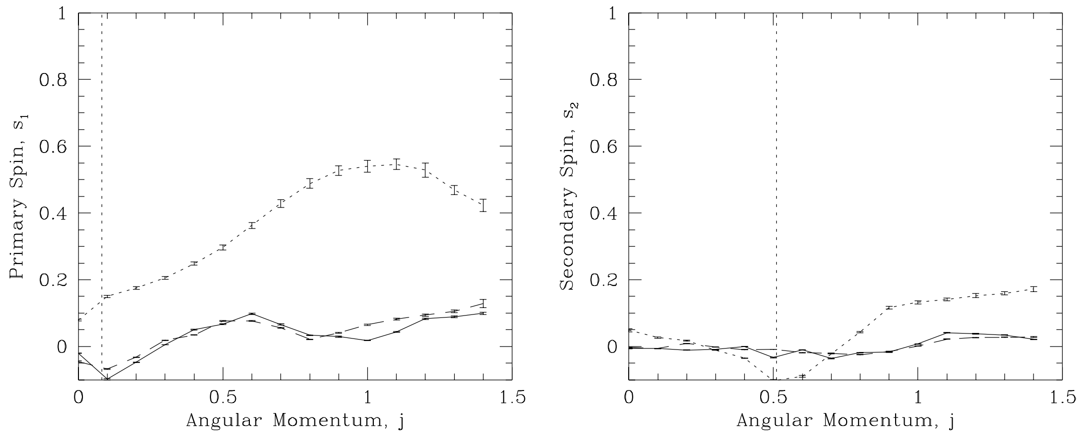

Figure 5.49: The specific spin angular momentum accreted by each of the binary components of a $q = 0.4$ binary. See Figure 5.46 for explanation.

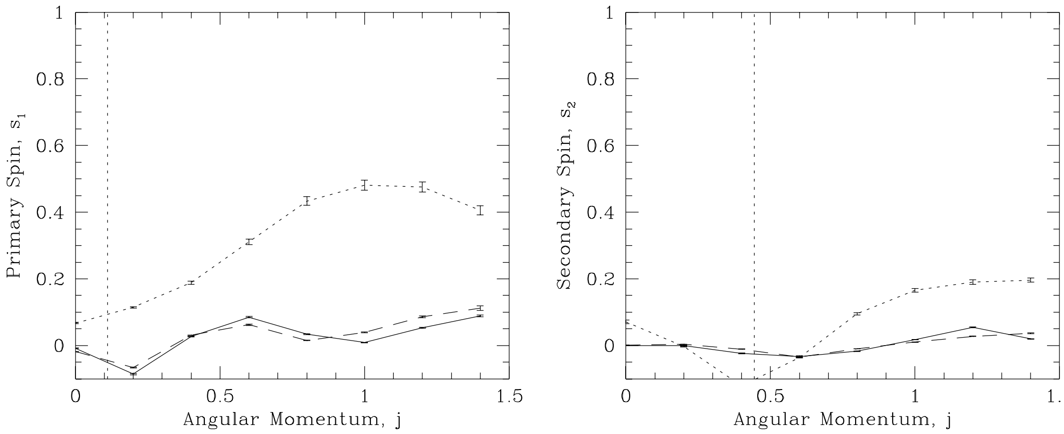

Figure 5.50: The specific spin angular momentum accreted by each of the binary components of a $q = 0.5$ binary. See Figure 5.46 for explanation.

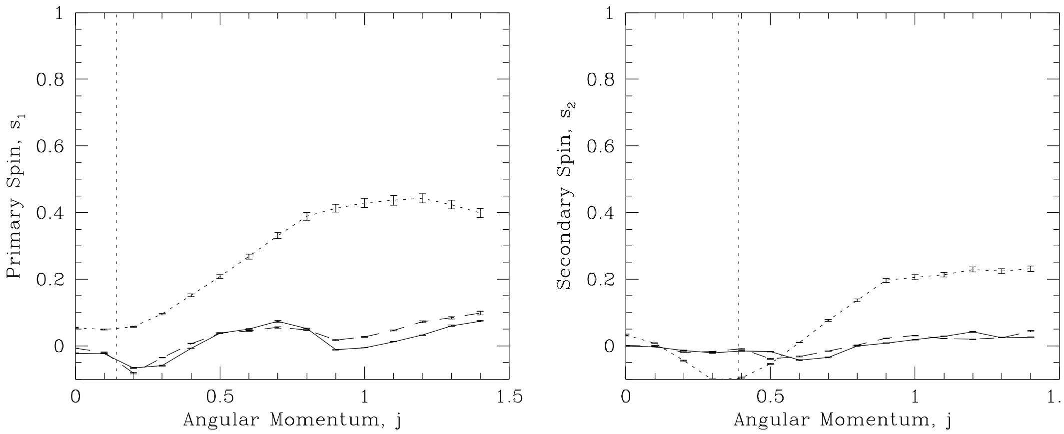

Figure 5.51: The specific spin angular momentum accreted by each of the binary components of a $q = 0.6$ binary. See Figure 5.46 for explanation.

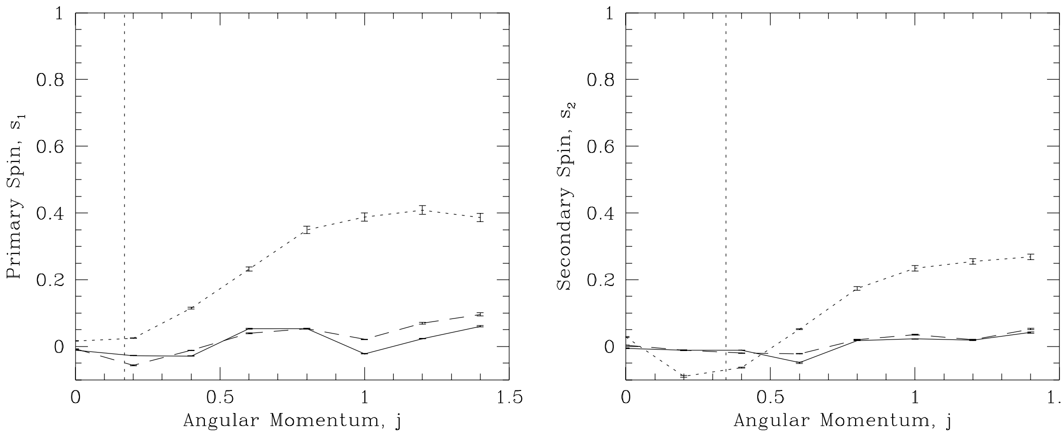

Figure 5.52: The specific spin angular momentum accreted by each of the binary components of a $q = 0.7$ binary. See Figure 5.46 for explanation.

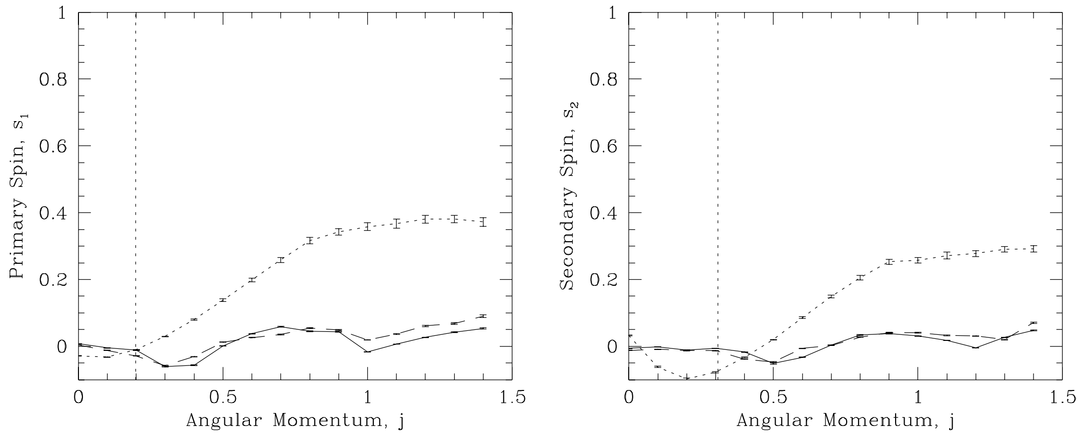

Figure 5.53: The specific spin angular momentum accreted by each of the binary components of a $q = 0.8$ binary. See Figure 5.46 for explanation.

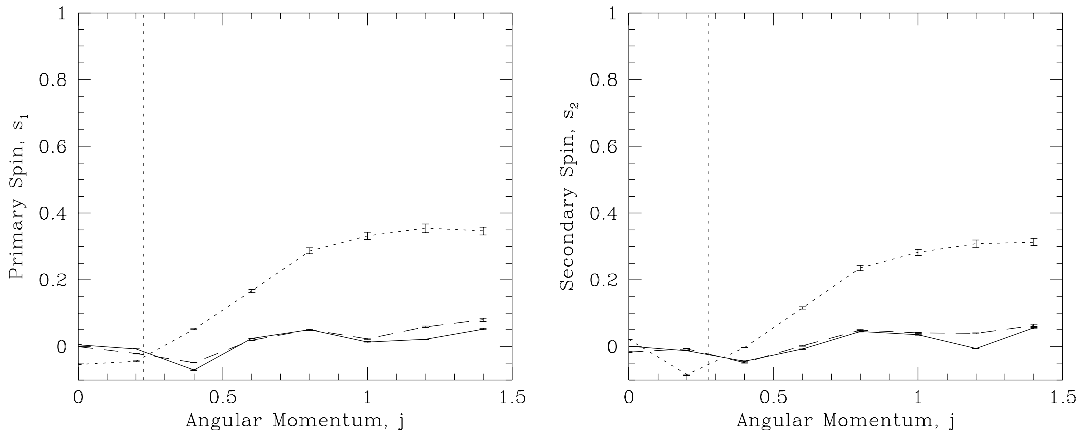

Figure 5.54: The specific spin angular momentum accreted by each of the binary components of a $q = 0.9$ binary. See Figure 5.46 for explanation.

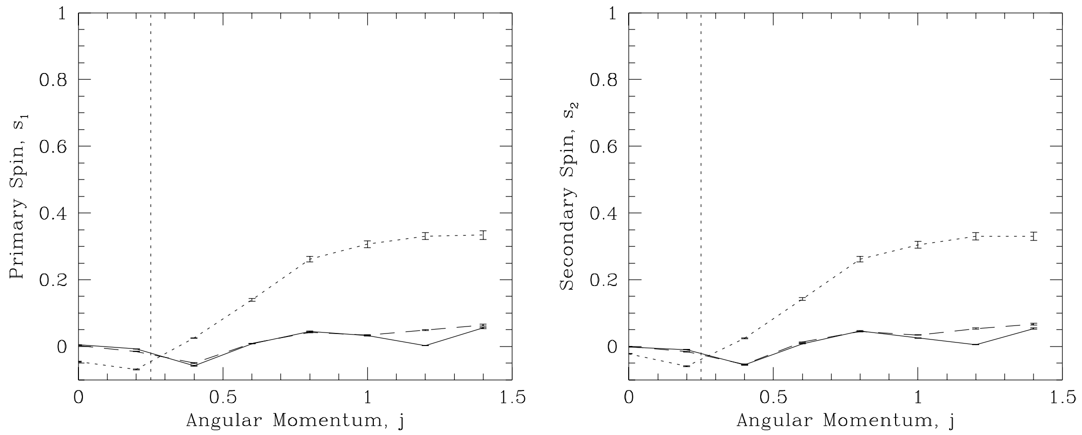

Figure 5.55: The specific spin angular momentum accreted by each of the binary components of a $q = 1.0$ binary. See Figure 5.46 for explanation.

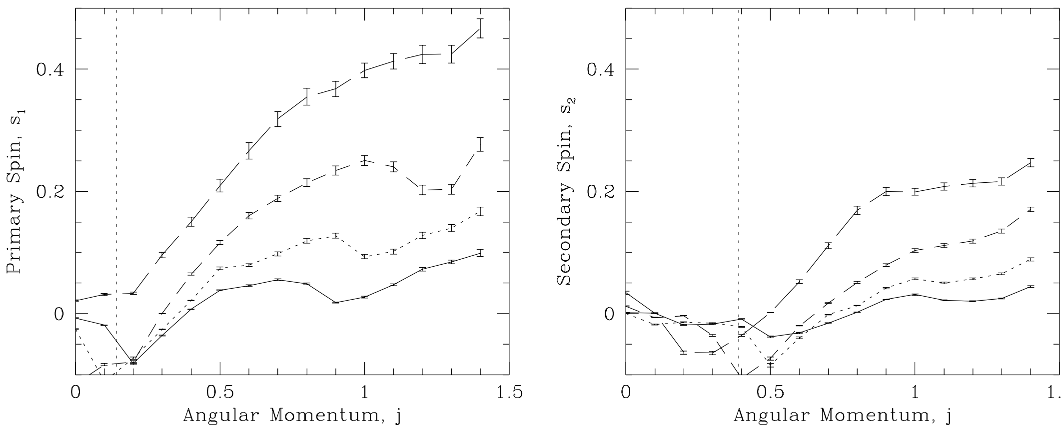

Figure 5.56: The specific spin angular momentum accreted by each of the components of a $q = 0.6$ binary. The graphs are plotted as a function of the specific angular momentum j of the infalling cloud, with $v_{\rm rad} = 0$, and for different protostellar accretion radii of $r_{\rm acc} = 0.05D$ (solid), $r_{\rm acc} = 0.10D$ (dotted), $r_{\rm acc} = 0.20D$ (short-dashed), and $r_{\rm acc} = 0.40D$ (long-dashed). The specific spin accreted by the primary s_1 (left), and the specific spin accreted by the secondary s_2 (right) are given. Estimated error bars are given. The vertical lines give the specific orbital angular momentum of the primary (left) and secondary (right).

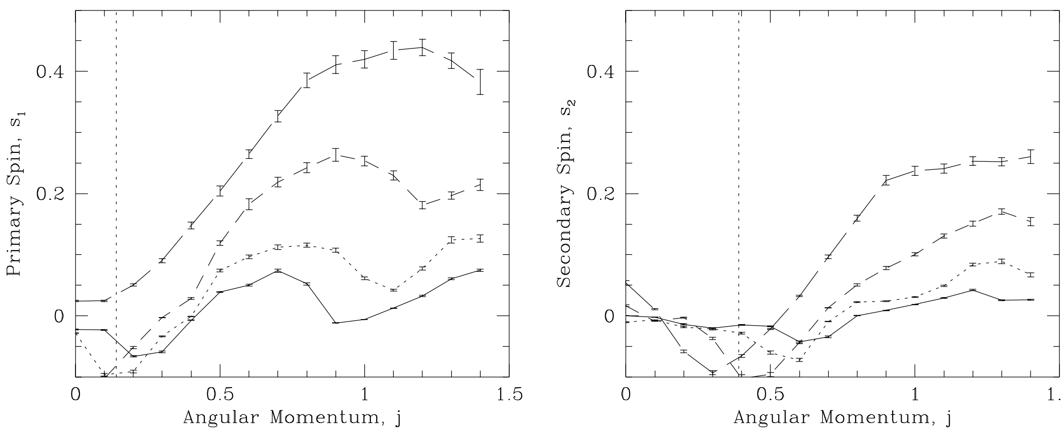

Figure 5.57: The specific spin angular momentum accreted by each of the components of a $q = 0.6$ binary with $v_{\rm rad} = 1$ with different protostellar accretion radii. See Figure 5.56 for explanation.

generally accrete far more spin angular momentum than the protostars of radius $r_{\rm acc} = 0.05D$. The progression is shown clearly in Figures 5.56 and 5.57 as the accretion radii of the protostars of a $q = 0.6$ binary are increased by a multiple of two for each series of calculations. All these figures also demonstrate that the accretion of spin angular momentum is insensitive of the initial radial-infall velocity at the outer boundary of the cloud.

Considering only the calculations performed with mean-Roche-lobe-sized protostars, the specific spin angular momentum of the accreted material varies greatly between the components for $q \neq 1$. For $q = 0.1$, the specific spin angular momentum accreted by the primary s_1 increases linearly with increasing j, until $j \approx 1$. However, the secondary accretes essentially **no** specific spin angular momentum, s_2! As the mass ratio is increased, s_1 decreases, but maintains a roughly linear increase with j up to $j \approx 1$. The linear increase for low j shows that a constant fraction of j is going into the spin of the primary. This fraction is different for different mass ratios because the accretion radius of the primary decreases with increasing mass ratio. For high j, the curves level off as the primary has a finite size which places an upper limit on the amount of spin angular momentum that a particle gives when it is accreted, for a constant velocity relative to the primary.

The secondary does accrete more specific spin angular momentum for higher mass ratios, and also displays a linear increase in specific spin angular momentum with increasing j, but in all cases (except $q = 1$) $s_2 < s_1$. This is because the accretion radius of the secondary is smaller than that of the primary, and the gas typically has a larger velocity relative to the primary than the secondary when it is captured. Also, for s_2 a critical value of j is apparent below which $s_2 \approx 0$. This critical value of j decreases with increasing mass ratio. A critical value of j is also apparent for the primary for high mass ratios, and the critical values of j converge for $q = 1$ when both components accrete appreciable amounts of spin angular momentum only for $j \gtrsim j_\mathrm{b}$ (Figures 5.46 to 5.55). The critical value of j above which positive spin angular momentum is accreted is given by

$$j \approx j_* \quad \text{where } j_* = \begin{cases} j_1 & \text{for the primary} \\ j_2 & \text{for the secondary.} \end{cases} \tag{5.14}$$

This is critical value arises because when a particle is accreted by a protostar it obtains the same specific orbital angular momentum as the protostar, by definition. If the accreted particle had less specific angular momentum than this before it was accreted, angular momentum is conserved by giving the protostar a retrograde spin. If the particle had a higher specific angular momentum than the protostar, the protostar receives prograde spin angular momentum.

If we assume that with gaseous accretion the infalling material follows roughly ballistic trajectories until the material enters the Roche lobes of the protostars, and only then is the kinetic energy of the gas dissipated, the mean-Roche-lobe-sized ballistic results presented here will give the specific spin angular momentum of the material that is captured by the protostars. In this case, the accreted spin effectively gives the sizes of the circumstellar discs. This hypothesis is tested in Chapter 6. It may also be possible for the secondary to form a retrograde disc in some cases, as the accreted material appears to have negative specific spin angular momentum relative to the cloud's specific angular momentum.

5.5 Conclusions

In conclusion, the effects of ballistic accretion on the masses and separations of initially-circular, protobinary systems have been studied for a wide range of mass ratios and values of the specific angular momentum of the infalling cloud. The qualitative behaviour of systems under ballistic accretion, determined by Artymowicz (1983), has been confirmed over this increased parameter space. First, the accretion of low-angular-momentum material decreases the mass ratio of the binary, while the accretion of high-angular-momentum material increases the mass ratio toward unity. Second, the accretion of low-angular-momentum material decreases the separation of the binary, while the accretion of high-angular-momentum material increases the separation.

Artymowicz found the quantitative results to be relatively insensitive to the initial radial-infall velocity of the material at the outer boundary of the calculation. The results presented here agree with this conclusion, with the exception of very high-angular-momentum infall. In this case, the radial-infall velocity of the infalling gas is critical in determining the relative accretion rate and thus the change in mass ratio of the binary. In most cases, the radial-infall velocity does not significantly affect the rate of change of separation of the binary.

Contrary to Artymowicz, the quantitative results are found to depend **critically** on the assumed sizes of the protostars. For large protostars, the relative accretion rates and rate of change of mass ratio are less extreme than for small protostars. Also, for large protostars, more of the accreted angular momentum is converted to spin angular momentum rather than orbital angular momentum, so that the rate of change of separation has lower values than for small protostars.

Thus, for these calculations to be used to predict the final state of a 'seed' binary under the accretion of its envelope, the appropriate sizes of the protostars must be determined. This is presumably some combination of the physical sizes of the protostars (for close binaries), and circumstellar disc sizes for more widely separated binaries. The only way to obtain these sizes is to include hydrodynamical effects in the calculations, as is done in the following chapter.

Finally, analysis of the specific spin angular momentum accreted by each of the components of a protobinary suggests that disc formation around the two components may differ considerably. If it is assumed that material travels ballistically until it enters the Roche lobe of one of the components, and then dissipates its excess energy to become bound to that component, then it appears that material around the primary nearly always has enough specific angular momentum to form a circumprimary disc. The material captured by the secondary, however, may not. The criterion for a protostar to accrete prograde spin angular momentum, in this case, is that the specific angular momentum of the infalling material be larger than the specific orbital angular momentum of the protostar $j \gtrsim j_*$. Whether or not this is how gaseous accretion behaves needs to be determined.

For the above reasons, gaseous accretion calculations are required to determine the quantitative behaviour of a 'seed' binary under accretion, although we now know what to expect from the ballistic calculations. They will also allow us to determine how much of the infalling material forms a circumbinary disc as a function of the specific angular momentum of the cloud, and how accretion from the circumbinary disc proceeds. This would be essential even if the ballistic calculations did give us the exact rates of change of mass ratio and separation and accreted spin angular momentum per unit mass accreted by the binary, because the amount of mass accreted by the binary, for a given infall rate, is not known. For high-angular-momentum infall some of the infalling material will not be accreted by the binary, but will end up in a circumbinary disc.